The galaxy database from the Vera Rubin Observatory, therefore, should be complemented with other galaxy catalogues to provide spectroscopic full-sky coverage as deeply as possible. From this point of view, several ongoing and planned galaxy surveys can be exploited. Currently, the largest spectroscopic galaxy surveys that are taking data are the Dark Energy Spectroscopic Instrument survey (DESI, from the ground, [1209]) and the ESA mission Euclid (from space, [1210]). DESI is planned to observe order of 10^7 galaxies at $0 < z < 3.5$ over $\sim$ 14000 square degrees, at a depth of 24, 23.4, and 23 for AB magnitudes g, r, and z, respectively; on the other hand, covering $\sim$ 14000 square degrees, Euclid will provide 1.5 billions photometric redshifts in the range $0 < z < 2$ and order of 30 millions spectroscopic redshifts at $0.84 < z < 1.88$, down to a Euclid H_E magnitude of 24. In the meanwhile, future spectroscopic surveys are already being planned and, pushing significantly deeper in redshift and completeness, they could constitute a fundamental resource to exploit the dark sirens provided by ET; in this respect, the most promising ones are the Wide-Field Spectroscopic Telescope (WST [1211]) and Spec-S5[22] facilities.

Besides utilising existing data, another possibility is performing dedicated galaxy surveys for the best localised GW events without a counterpart to maximise their impact on the dark siren method. In parallel to that, dedicated spectroscopic follow-up surveys could be conducted for the best-localized events.

Formally, dark sirens analyses are conducted with a hierarchical Bayesian approach [1212–1214], which allows the propagation of uncertainties on the individual events to the population properties. Crucially, when using the population properties to infer cosmology, one must take into account the fact that those are actually unknown, but determine the selection bias of the experiment, which needs to be carefully deconvolved to obtain unbiased estimates of the cosmological parameters. This is usually done with large injections campaigns to determine the sensitivity of the instrument to the targeted population [1215–1217]. The scaling of this technique to ET needs to be assessed, both in terms of accuracy and computational cost. Furthermore, the likelihood evaluation, involving the computation of multi-dimensional Monte Carlo integrals at each iteration to marginalize over the individual source properties and/or the construction of redshift priors from the interpolation of large galaxy catalogs, is computationally demanding. Alternative approaches such as simulation-based [1218] and/or machine-learning leveraged pipelines [1219] and/or GPU-accelerated codes [1220], might be beneficial for tackling these challenges.

We can identify several milestones that ET can bring in this context, regardless of the technical details. The construction of a redshift prior from galaxy catalogs benefits in particular from the accurate sky localization.[23] Figure 47 shows the localization capabilities of ET in the triangular and 2L configurations.[24] In particular, we show the 90% sky localization area as a function of redshift, while the color refers to the number of galaxies contained in the localization volume, assuming a constant galaxy density of 10^{-2} galaxies/Mpc^3. In particular, ET has the potential of localizing $\mathcal{O}(10^3)$ sources per year to better than 10 deg^2 [16]. Remarkably, figure 47 also shows that ET alone could allow pinpointing the host galaxy of

[22] See https://www.spec-s5.org/pubs/.

[23] Similar arguments hold for the cross-correlation of resolved sources with other tracers of the LSS, see section 3.4.1, as well as for the identification of a direct counterpart, see section 3.3.1.1.

[24] We refer to ref. [16] for the details on the catalogs, software, and detector shape and orientations used.

JCAP03(2026)081

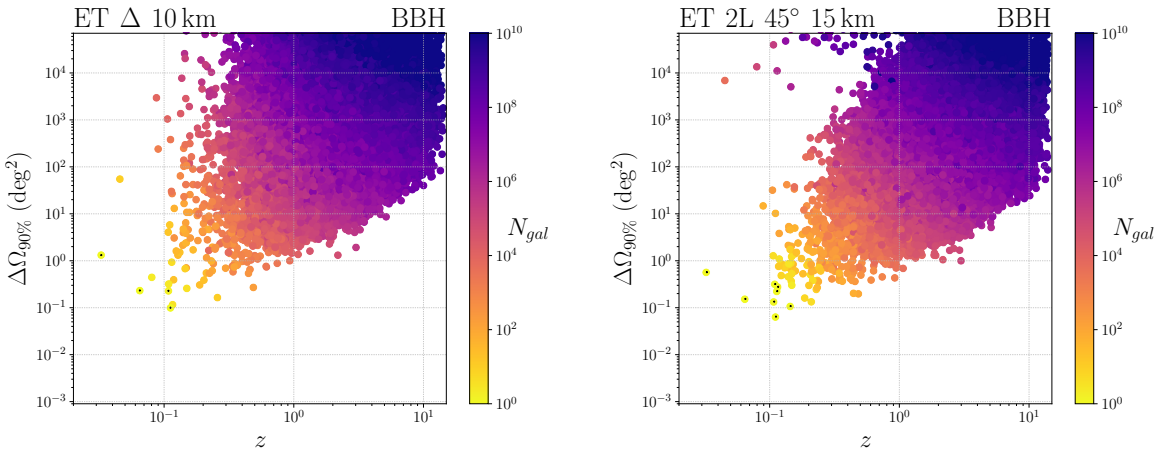

Figure 47. Localization capabilities for BBHs of ET in its triangular (left panel) and 2L-15km-45° (right panel) configurations. The color scale denotes the number of galaxies expected in the 90% localization volume. Events marked with black dots are localized to one galaxy only.

the merger at a rate of a few per year without the need of a direct EM counterpart. Events with a single host galaxy are further marked with a black dot in figure 47. This scenario alone would lead to a determination of the Hubble constant, and is a unique possibility of ET. Figure 48 shows the number of galaxies enclosed in the GW localization volume of ET golden BBH events (i.e., with $\Delta\Omega < 2\,\mathrm{deg}^2$) in the triangular and 2L configurations using the catalog of massive MICEcat galaxies, as in [1147]. In particular, ET has the potential of localizing $\mathcal{O}(10^2)$ sources per year to better than $2\,\mathrm{deg}^2$ [16]. We note that, besides cosmology, this could bring invaluable information about the relation between galaxy properties and GW emission [1203]. Indeed, assigning a weight to galaxies according to their properties such as mass or star formation rate can help increasing the accuracy on H_0 when using also GW sources with a large number of galaxies in their localization volume [9, 1143]. However, the dependence on the galaxy properties will have to be correctly modeled and marginalized over, in order to avoid systematics [1203].

Besides subsamples of "golden" events, as already remarked, it is important to stress that ET will detect almost the entire population of BBHs below the star formation peak, and more than 90% of BBHs of stellar origin across all redshifts [16, 1167]. In this large-statistics regime, information from sources with poorer sky localization will still contribute to reconstruct precisely the source-frame mass distribution, hence to determine cosmology [1157]. In this context, the possible systematics related to the correct modeling of source-frame features [1200], and their correlation to redshift evolution [1221], will need to be addressed. However, we stress that the presence of features in the mass spectrum can in principle be inferred directly from data, without the need of a specific modeling, using non-parametric approaches [1221–1223]. This will allow a robust measurement of the cosmic expansion history.

Love Sirens. Neutron stars taking part in compact binary coalescences, whether as BNS or NSBH systems, undergo tidal deformation during the later stages of the inspiral process. The tidal deformability parameter (Λ) is related to the compactness ($\mathcal{C}$) of the neutron star

JCAP03(2026)081

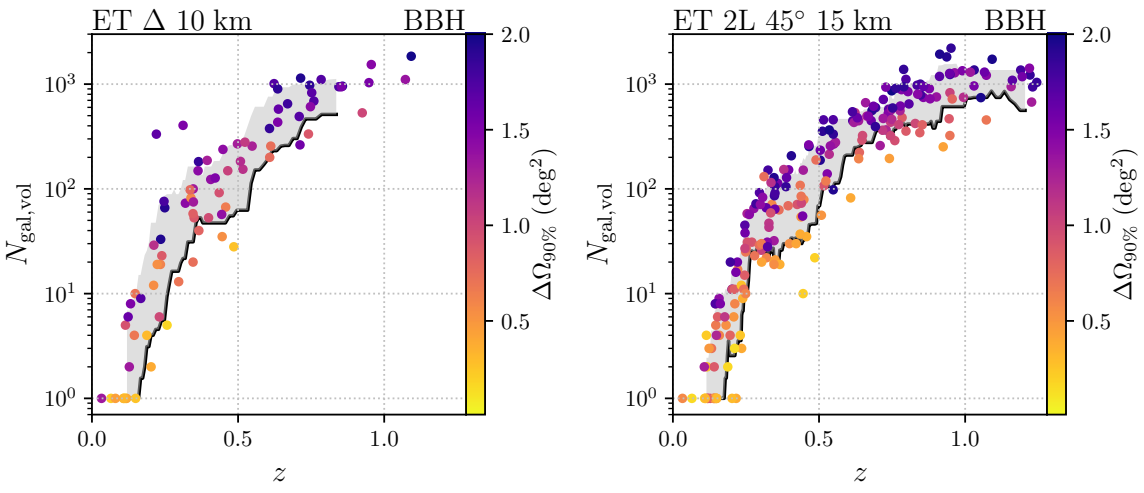

Figure 48. Number of galaxies inside the localization volume of ET golden BBH events ($\Delta\Omega < 2\,\mathrm{deg}^2$) for the triangular (left) and 2L (right) configuration. The color bar represents the 90% sky localization area. The black line and shaded region indicate the 16th and 84th percentiles, respectively.

via the second tidal Love number (k_2) by,

$$\Lambda = \frac{2}{3} k_2 \mathcal{C}^{-5}, \tag{3.70}$$

where $\mathcal{C} = m/R$, where R is the radius of the NS and m its source-frame mass [1224]. The parameters k_2 and $\mathcal{C}$ depends on the equation of state governing the NS (see section 7 for details). These deformations leave an imprint on the GW amplitude and phase; in particular, the dominant effect of tidal deformation appears in the phase at the fifth post-Newtonian order, characterized by a combination of the individual tidal deformability parameters (note that $\Lambda = 0$ for BHs) and the mass ratio of the binary [1225]. This combination, called the reduced tidal deformability $\tilde{\Lambda}$ (see eq. (7.5) or eq. (10.18) for the explicit expression), is the best-measured tidal parameter using GW. The next-to-leading order contribution to the GW phase is characterized by another linear combination of individual Λs and the mass ratio, denoted by $\delta\tilde{\Lambda}$, see eq. (10.18). The contribution of $\delta\tilde{\Lambda}$ to the phase is subdominant compared to that of $\tilde{\Lambda}$, even at the sixth post-Newtonian order, which is why it is not expected to be constrained very well with GW observations. Furthermore, if the neutron stars are spinning, the individual Λs also contribute to the phase from spin-induced quadrupolar deformations which appear at the 2.5 post-Newtonian order and beyond [1226–1229]. Given these effects, one can constrain the individual tidal deformability of the two compact objects using GW detections, as we detail in section 7.

With an established NS equation of state, inferred Λ can be converted to constraints on source-frame mass using eq. (3.70). As GW observations also provide precise constraints on detector-frame mass, the measured detector-frame mass can be compared to the inferred source-frame mass, giving constraints on the redshift associated with the source [1140]. Together with the measurement of the luminosity distance d_L obtained from the GW signal, one can then obtain measurements of the cosmological parameters. Furthermore, exploiting

JCAP03(2026)081

the post-merger signals of BNS mergers can enable the resolution of redshift-mass degeneracy by exploiting spectral features dependent on the source-frame masses of the binary [1230]. This method, which leverages the constraints on tidal deformability parameters, knowledge of the neutron star equation of state, and, possibly, the spectral features from neutron star post-merger, to break the mass-redshift degeneracy and obtain a redshift estimate, is referred to as the Love siren approach.

If using only the inspiral part of the signal, the redshift constraints obtained using the Love siren method depend on the precision with which $\tilde{\Lambda}$ and the detector-frame masses are inferred. The sensitivity improvement in ET at both low and high frequencies greatly improves these two measurements. Specifically, for $\mathcal{O}(100)$ BNS events detected with the triangular ET configuration every year, the fractional error in $\tilde{\Lambda}$ is expected to be less than 10% and that in chirp mass is expected to be less than $\mathcal{O}(10^{-5})$ [1167]. With the 2L-45° geometry, this number can increase to $\mathcal{O}(10^3)$ every year [1231]. With the triangular ET geometry, the redshift can be measured with a precision of $\mathcal{O}(10\%)$ for systems up to $z \sim 1$ [1140, 1232, 1233]. With the post-merger spectra, this can be achieved for systems up to $z \sim 0.04$ [1230]. In fact, the post-merger signal for a BNS system can be detected with an SNR of 10 for systems up to $\sim 90\,\mathrm{Mpc}$ with ET alone, resulting in $\mathcal{O}(1\%)$ measurement of the post-merger peak frequency f_2 [1234]. Together with CE, the redshift can be resolved to $\sim 1\%$ for $\mathcal{O}(10^4)$ yearly detections, which translates to 0.1% error in H_0 and 0.61% error in Ω_m in a year of observation [1235] (see also [1236, 1237]).

The Love siren method represents an approach to cosmological parameter estimation that only relies on the GW signal, requiring a robust understanding of the neutron stars equation of state, expected to be significantly enhanced by forthcoming observatories [107, 1231, 1238, 1239]. An equation of state agnostic approach can also be used, that jointly estimates the equation of state and the cosmological parameters [1240]. However, caution is warranted in post-merger spectrum-based forecasts, which require improved modeling of gravitational waves from hypermassive neutron star remnants.

3.3.1.3 Cosmic dipole tension. The Earth's motion relative to the Hubble flow generates a dipole anisotropy in both the temperature of the CMB [590, 591, 1241] and in the angular distribution of electromagnetic sources observed at cosmological distances [1242–1244]. This type of angular anisotropy is typically called the "cosmic dipole". There is currently a $\sim 5\sigma$ tension between the estimation of the cosmic dipole from the early Universe (CMB) and the one inferred from the angular distribution of active galactic nuclei (AGN) [591, 1242]. It has been argued that this tension might be alleviated by modeling the redshift evolution of radio sources [1245], however, nowadays this tension is still open for debate (see also the discussion in [1246] and the references therein).

GW sources observed with 3G detectors offer a new avenue to solve this cosmic dipole tension. The cosmic dipole could be estimated from the stochastic GW backgrounds generated by cosmological and astrophysical sources (see section 3.1.1 for more details), but can also be estimated from the angular distribution of GW sources [1247, 1248]. ET embedded in a detector network with CE will provide $\sim 3 \cdot 10^4$ BBH sources per year with a 90% localization area lower than $10\,\mathrm{deg}^2$. The angular distribution of these well-localized sources can be used to detect and estimate the cosmic dipole.

JCAP03(2026)081

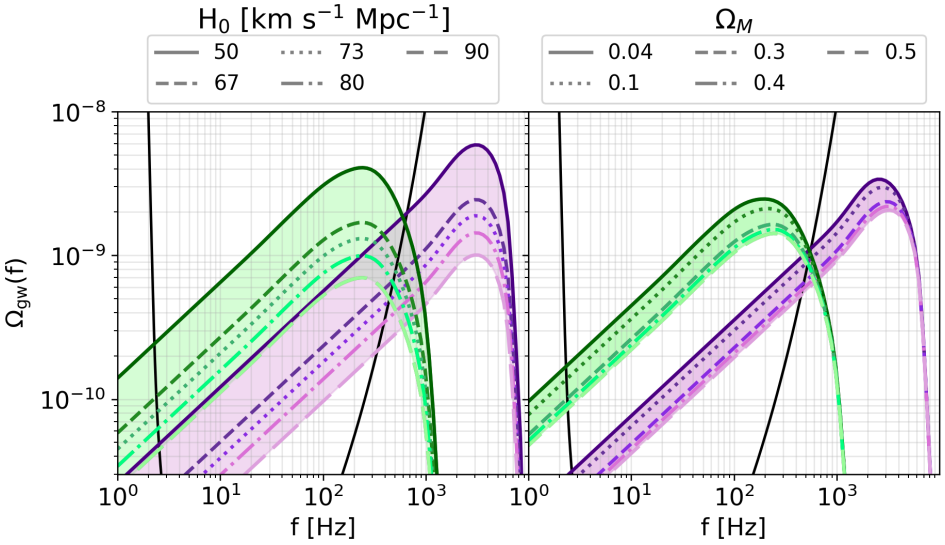

Figure 49. Effect of varying the value of H_0 and Ω_M on the energy density of the stochastic background from BBHs (green) and BNSs (purple). The astrophysics is fixed to the models described in [551, 1249]. The black curve is the PLS of ET for the triangular 10 km configuration [16].

By considering the angular number density of GW sources, with just 2–3 years of observations, 3G detectors have a 75% probability of detecting the cosmic dipole if its value is consistent with the one inferred from AGN [1247]. The probability of detecting the dipole increases to 100% if we consider 10 years of joint observations. Therefore, with just few years of observations, there is the concrete possibility of ruling out the AGN value of the cosmic dipole and solving this tension. The possibility of detecting and measuring the cosmic dipole are enhanced if also binary neutron star (BNSs) sources are considered. For this class of sources, it is also possible to inspect the presence of a cosmic dipole by studying the angular dependence of the detector-frame mass spectrum of BNSs, which is also expected to be modified by the cosmic dipole. Including BNSs and the angular distribution of the detector-frame mass spectrum, it will be possible to enhance the probability of detecting the cosmic dipole by 30–50% [1248] for a given observing time, thus making the detection of an AGN cosmic dipole in just 2–3 years of observation almost certain.

Furthermore, as discussed in detail in section 3.1.2.2, in [555] it has been shown that a detection of the dipole of the AGWB at different frequencies with ET and CE would allow to measure the dipole of the AGWB emitted by BBH and to distinguish between the kinematic, intrinsic and shot noise contributions, see figure 21 for more details. The component separation of the dipole of the AGWB which could be done by ET and CE is crucial to understand if the cosmic dipole tension is due to a relative velocity between the CMB and LSS frame (by comparing the CMB and AGWB kinetic dipoles) or to an anomalous intrinsic dipole of the CMB or LSS.

3.3.1.4 The astrophysical background as a cosmological probe. Another observable that can be used to constrain cosmological parameters with ET is the astrophysical GW background (AGWB) produced by coalescing binaries. The frequency spectrum of the

JCAP03(2026)081

AGWB is determined by the complex interplay of various astrophysical factors, as discussed in section 4, but also by the underlying cosmology. The region of the spectrum which contains most of the information is the high-frequency peak, whose shape and position are very sensitive to all the various astrophysical and cosmological factors at play. For instance, in figure 49 we show the effect of varying the value of the Hubble parameter and the matter density parameter on the peak of the AGWB produced by BBHs and BNSs. With the sensitivity of ET in the 1–100 Hz range, the frequency spectrum of the astrophysical GWB will be measured precisely. This, in turn, will open the possibility for a Bayesian reconstruction of both astrophysical and cosmological parameters, in line with the methodology outlined in [1250] for the specific case of the GWB from BNSs. This approach complements existing methods such as GW sirens, discussed in the previous sections, which constitute the main strategy to constrain cosmological parameters with GWs. By employing these techniques concurrently, it becomes feasible to mitigate degeneracies and potentially refine parameter constraints further, particularly if posterior contours are orthogonal.

3.3.2 Modified GW propagation

3.3.2.1 Observables for the dark-energy sector. In ΛCDM, on sufficiently large scales where cosmological perturbation theory applies, one performs a separation between a homogeneous Friedmann-Lemaitre-Robertson-Walker (FLRW) background, and scalar, vector and tensor perturbations over it. Whenever gravity is modified on cosmological scales, both the background evolution and scalar and tensor perturbations are modified (while, in ΛCDM and in most modified gravity models, vector perturbations usually only have decaying modes and are irrelevant). At the level of the background evolution, the effect of modified gravity is encoded in a dark energy (DE) density $\rho_{\rm DE}(z)$ and a DE pressure $p_{\rm DE}(z)$. One can then introduce the DE equation of state $w_{\rm DE}(z)$, defined by $p_{\rm DE}(z) = w_{\rm DE}(z)\rho_{\rm DE}(z)$; ΛCDM is recovered for $w_{\rm DE}(z) = -1$. Using the conservation of the DE energy-momentum tensor, one finds that the DE density is given as a function of redshift by

$$\rho_{\rm DE}(z) = \rho_0 \Omega_{\rm DE} \exp\left\{3\int_0^z \frac{d\tilde{z}}{1+\tilde{z}}\left[1+w_{\rm DE}(\tilde{z})\right]\right\}, \tag{3.71}$$

where $\Omega_{\rm DE} = \rho_{\rm DE}(0)/\rho_0$ is the DE density fraction and $\rho_0 = 3H_0^2/(8\pi G)$ is the critical density today. At the background level, the properties of DE are therefore encoded just in one function $w_{\rm DE}(z)$. The corresponding expression for the luminosity distance is

$$d_L(z) = \frac{c}{H_0}(1+z)\int_0^z \frac{d\tilde{z}}{\sqrt{\Omega_{\rm M}(1+\tilde{z})^3 + \Omega_{\rm R}(1+\tilde{z})^4 + \rho_{\rm DE}(\tilde{z})/\rho_0}}, \tag{3.72}$$

where $\Omega_{\rm M}$ is the present matter fraction and $\Omega_{\rm R}$ that of radiation (which we have written for completeness, but is completely negligible at the redshifts where astrophysical compact binaries merge; we also write for simplicity our equations for a flat cosmology, so $\Omega_{\rm M} + \Omega_{\rm R} + \Omega_{\rm DE} = 1$). When $w_{\rm DE} = -1$, $\rho_{\rm DE}$ in eq. (3.71) becomes a constant, that we denote ρ_Λ, and eq. (3.72) reduces to the ΛCDM expression

$$d_L(z) = \frac{c}{H_0}(1+z)\int_0^z \frac{d\tilde{z}}{\sqrt{\Omega_{\rm M}(1+\tilde{z})^3 + \Omega_{\rm R}(1+\tilde{z})^4 + \Omega_\Lambda}}, \tag{3.73}$$

JCAP03(2026)081

where $\Omega_\Lambda = \rho_\Lambda/\rho_0$. At low redshift, both eq. (3.72) and eq. (3.73) reduce to Hubble's law $d_L(z) \simeq (c/H_0)z$, so standard sirens at low redshift allows us to measure H_0. At the redshifts accessible to ET, however, we can also test the DE equation of state, and any deviation from the ΛCDM value $w_{\rm DE} = -1$ would provide evidence for a dynamical dark energy. In general, however, it is difficult to extract from the data a full function of redshift, such as $w_{\rm DE}(z)$, and a parametrization in terms of a small number of parameters is useful. For the DE equation of state a standard choice is the (w_0, w_a) parametrization [1251, 1252],

$$w_{\rm DE}(z) = w_0 + \frac{z}{1+z} w_a \,. \tag{3.74}$$

The evolution of the cosmological background can be tested both with standard electromagnetic cosmological probes, such as CMB, Supernovae, Baryon Acoustic Oscillations (BAO) or structure formation, and by GW observations, combining the GW measurement of the luminosity distance of coalescing binaries with information on the redshift, obtained either with an electromagnetic counterpart, if it is observed ("standard sirens") or with statistical methods ("dark sirens"), as discussed in section 3.3.1. A first observable for GW observations, in the context of dark energy and modified gravity, is therefore the DE equation of state $w_{\rm DE}(z)$ or, more simply, the two parameters (w_0, w_a). Modifications of the cosmological model in the sector of scalar perturbations are less directly relevant for GW experiments, and rather manifest themselves in cosmological structure formation; these modifications are among the targets of current galaxy surveys. However, for GW observation, there are further quantities that are accessible, to test modified gravity: GW observation can in fact access modifications in the tensor perturbation sector (i.e., GWs propagating over a FLRW background). In GR the equation that governs the propagation of tensor perturbations over FLRW is given by

$$\tilde{h}_A'' + 2\mathcal{H}\tilde{h}_A' + c^2 k^2 \tilde{h}_A = 0 \,, \tag{3.75}$$

where $\tilde{h}_A(\eta, \mathbf{k})$ is the Fourier-transformed GW amplitude, $A = +, \times$ labels the two GW polarizations, the prime denotes the derivative with respect to cosmic time η [defined by $d\eta = dt/a(t)$], $a(\eta)$ is the scale factor, and $\mathcal{H} = a'/a$. In modified gravity theories, this propagation equation is modified, as has been found on many explicit modified gravity models [66, 1253–1262]. A modification of the coefficient of the $k^2\tilde{h}_A$ term induces a speed of GWs, $c_{\rm gw}$, different from that of light. After the observation of GW170817, this is now excluded at a level $|c_{\rm gw} - c|/c < \mathcal{O}(10^{-15})$ [3] (at least for scale-independent modifications, see [1263]). However, the modified gravity models that pass this constraint still, in general, induce a change in the above equation, that becomes

$$\tilde{h}_A'' + 2\mathcal{H}[1 - \delta(\eta)]\tilde{h}_A' + c^2 k^2 \tilde{h}_A = 0 \,, \tag{3.76}$$

for some function $\delta(\eta)$ that encodes the modifications from GR. As a result, the amplitude of a GW propagating across cosmological distances, from the source to the observer, is modified, because of this different friction term; one can then show that the amplitude of the GW from a coalescing binaries no longer allows us to obtain the standard luminosity distance $d_L(z)$ of the source [that, in this context, we will denote by $d_L^{\rm em}(z)$, since this is the quantity that would be measured, for instance, using the electromagnetic signal from

JCAP03(2026)081

a counterpart]. Rather, the quantity extracted from GW observation is a "GW luminosity distance" $d_L^{\rm gw}(z)$ [1257], related to $d_L^{\rm em}(z)$ by [1257, 1259]

$$d_L^{\rm gw}(z) = d_L^{\rm em}(z) \exp\left\{-\int_0^z \frac{dz'}{1+z'}\,\delta(z')\right\}\,, \tag{3.77}$$

where the function δ that appears in eq. (3.76) has now been written as a function of redshift.

Of course, to perform a full inference on the function $\delta(z)$ from future GW data is difficult (although it can be performed, to some extent, with the technique of Gaussian process reconstruction [1170]) and, similarly to what is done for the DE equation of state, it is convenient to introduce a parametrization. A very convenient choice, proposed in [1259], takes the form

$$\frac{d_L^{\rm gw}(z)}{d_L^{\rm em}(z)} = \Xi_0 + \frac{1-\Xi_0}{(1+z)^n}\,, \tag{3.78}$$

in terms of two parameters (Ξ_0, n). This parametrization interpolates, with a power-law in the scale factor $a = 1/(1+z)$, between $d_L^{\rm gw}/d_L^{\rm em} = 1$ at $z = 0$ (i.e. when there is no propagation), and a constant value large redshifts; the latter limit is motivated by the fact that, in typical modified gravity models, the deviations from GR only appear in the recent cosmological epoch, so $\delta(z)$ goes to zero at large redshift, and the integral in eq. (3.77) saturates to a constant; GR corresponds to $\Xi_0 = 1$ (for any n). This simple parametrization has been shown to work remarkably well for practically all best-studied modified gravity models [1262] (except bigravity, where $d_L^{\rm gw}/d_L^{\rm em}$ displays some oscillations).

Another parametrization of modified GW propagation which has been used in the literature is given by

$$\alpha_M(z) \equiv -2\delta(z) = c_M \frac{\Omega_{\rm DE}(z)}{\Omega_{\rm DE}}\,, \tag{3.79}$$

where c_M is a constant and $\Omega_{\rm DE}(z) = \rho_{\rm DE}(z)/\rho_0$. This parametrization was introduced in [1264] to study the scalar sector of Horndeski theories and, in these theories, it turns out that the same function also describes the modification of the tensor sector. A drawback of the parametrization (3.79) is that it requires to postulate an expression for $\Omega_{\rm DE}(z)$, i.e. for $\rho_{\rm DE}(z)$, so it is less suitable for model-independent studies. In practice, when applied to modified GW propagation, this parametrization has been used assuming that the dark energy density is constant, $\rho_{\rm DE}(z) = \rho_{\rm DE}(0)$ [1265, 1266] (which, however, is not expected to be the case, since if the tensor sector of the theory is modified with respect to ΛCDM, also the background evolution will be different). In any case, as long as $\Omega_{\rm DE}(z)$ is such that the integral in eq. (3.77) saturates to a finite value (which is also the case of a constant $\Omega_{\rm DE}$), this parametrization is still qualitatively of the same form as eq. (3.78), since the ratio $d_L^{\rm gw}(z)/d_L^{\rm em}(z)$ goes from unity at $z = 0$ to a constant Ξ_0 at large z. However, this parametrization is less general than the (Ξ_0, n) parametrization, since it only has one parameter, c_M, so it implicit assumes a relation between Ξ_0 and n (see appendix F of [1154] for detailed comparison). Other proposed parametrizations include

$$\Xi(z) = \sqrt{\frac{1+\Omega_0}{1+\Omega_0 a^\beta}}\,, \tag{3.80}$$

JCAP03(2026)081

from [1267], which has the same behavior as that of eq. (3.78) when the deviations from GR are small ($|\Omega_0| \ll 1$), with the correspondence $\Xi_0 = 1 + \Omega_0/2$ and $n = \beta$; also

$$\alpha_M(z) = \alpha_{M0} a^\beta \quad (\beta > 0)\,, \tag{3.81}$$

used in the context of the EFT of dark energy [591, 1268]; and the one of [1269].

It is interesting to note that, with electromagnetic observations, the background evolution and the scalar perturbations have been tested to a few percent level. For instance, combining many different cosmological datasets (and setting $w_a = 0$), one finds $w_0 = -1.031^{+0.030}_{-0.027}$ [1270], consistent with ΛCDM at the 3% level (although the recent DESI results [1271], even if consistent with a flat ΛCDM model, when combined with other datasets prefer an evolving dark energy equation of state with phantom crossing below $w = -1$ at redshift $z \simeq 0.4$), while for the parameters Σ_0 and μ_0 that parametrize deviations in the scalar perturbation sector (with $\mu_0 = \Sigma_0 = 0$ in GR) one finds $\mu_0 = -0.04 \pm 0.25$ and $\Sigma_0 = -0.024 \pm 0.054$ [1272], so the latter corresponds to a test of GR and ΛCDM at the 5% level. Naively one would then imagine that, if a modified gravity model complies with existing bounds in the background evolution and in the scalar perturbation sector, even in the tensor perturbations its deviation from GR will not exceed a few percent. Indeed, this is true for some important classes of models, like the $f(R)$ or several scalar-tensor theories, where the GW friction is the time variation of the effective Planck mass,

$$\alpha_M(z) = \frac{d \log M_*^2}{d \log a}\,. \tag{3.82}$$

There, α_M is also sourcing gravitational slip $\eta \equiv \Phi/\Psi = 2\Sigma/\mu - 1$ [1253, 1264, 1267], therefore linking tests of gravity based on standard sirens with those from large-scale structure. However, this link is not generally true; as an explicit example, the model originally proposed in [64] complies with all observational limits in the background evolution and in the scalar sector but, in the tensor sector, predicts a value of Ξ_0 that (depending on a free parameter related to initial conditions) can be as large as 1.8 [66], corresponding to a 80% deviation from GR. Figure 50, from ref. [66], shows the prediction for $\delta(z)$ (left panel) and $d_L^{\rm gw}/d_L^{\rm em}$ in this non-local model, for different values of a free parameter of the theory (see [66] for details).

This shows that the window of cosmological tensor perturbations, that has been opened for the first time by the LVC and LVK observations, and that will be deeply explored by ET, is extremely interesting and could reserve us remarkable surprises.

3.3.2.2 Current limits on Ξ_0. Using the various methods for bright and for dark sirens discussed previously in this chapter, several limits on modified GW propagation have already been obtained from the current dataset of GW detections.

A first limit was obtained in [1259] using GW170817 as a standard siren with counterpart (see also [1265]). In this case the electromagnetic luminosity distance of the host galaxy can be obtained from surface brightness fluctuations. Because of the very small redshift of GW170817, what is obtained is really a limit on $\delta(z = 0)$, independently of the parametrization used, and the result from [1259] is $\delta(0) = -7.8^{+9.7}_{-18.4}$. In terms of Ξ_0, this corresponds to a rather broad limit $\Xi_0 \lesssim \mathcal{O}(10)$. This limit is not stringent because GW170817 has a very small redshift, $z \simeq 0.01$, and the effect of modified GW propagation disappears as $z \to 0$.

JCAP03(2026)081

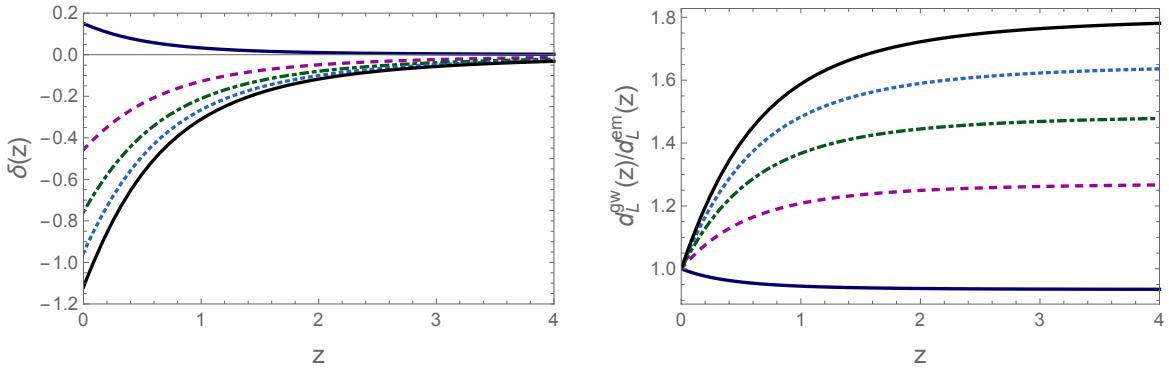

Figure 50. The functions $\delta(z)$ (left panel) and $d_L^{\rm gw}(z)/d_L^{\rm em}(z)$ (right panel), for the non-local gravity model proposed in [64], for different values of a free parameter of the theory. Reproduced from [66], © 2020 IOP Publishing Ltd and Sissa Medialab. All rights reserved.

A stronger bound was obtained in [1143] using BBH dark sirens from the O1, O2 and O3a LIGO/Virgo run, and performing a correlation with the GLADE [1186] galaxy catalog. This gives (at 68% c.l.)

$$\Xi_0 = 2.1^{+3.2}_{-1.2}\,. \tag{3.83}$$

A more stringent bound can obtained if one accepts the tentative identification of the flare ZTF19abanrhr as the electromagnetic counterpart of the BBH coalescence GW190521, as proposed in [1273].[25] Then, the analysis in [1143] (keeping fixed H_0 to the Planck value) gives

$$\Xi_0 = 1.8^{+0.9}_{-0.6}\,, \tag{3.84}$$

(68% C.L.). A similar results is obtained in [1275], again assuming the identification of ZTF19abanrhr with GW190521, and combining this with GW170817. Using again a narrow prior on H_0 the most stringent limit obtained in [1275] (for different choices of the waveform) is $\Xi_0 < 2.9$.

Another approach is to constrain modified GW propagation using the BBH mass distribution, following the strategy proposed in [1153]. Using the BBH mass function and the GWTC-3 catalog, ref. [1154] finds

$$\Xi_0 = 1.2^{+0.7}_{-0.7}\,, \tag{3.85}$$

with a flat prior on Ξ_0, and $\Xi_0 = 1.0^{+0.4}_{-0.8}$ with a prior uniform in $\log \Xi_0$, while using the GWTC-2 catalog of GW events and the parametrization (3.79) with a constant $\rho_{\rm DE}$, ref. [1266], finds $c_M = -3.2^{+3.4}_{-2.0}$ (see appendix G of [1154] for a discussion of the technical differences between the analyses of refs. [1266] and [1154]).

[25] In [1274] it was observed that the volume localization of GW190521 is not statistically sufficient for a confident identification of ZTF19abanrhr as the electromagnetic counterpart. However, this assumes no modified GW propagation. Introducing the possibility of modified GW propagation has precisely the effect of restoring the consistency between the volume localization of GW190521 and the flare ZTF19abanrhr.

JCAP03(2026)081

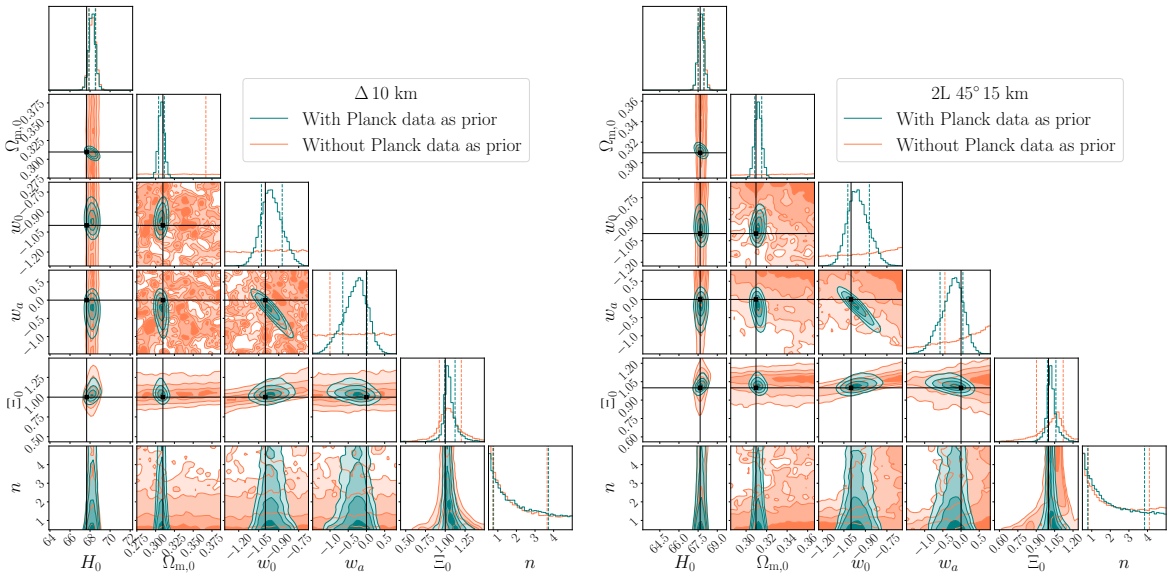

Figure 51. Results of the joint inference on the cosmological parameters H_0, $\Omega_{\mathrm{m},0}$, w_0, w_a, Ξ_0 and n employing GW+KN events detected in one year of observations by the 10 km triangular (left panel) and the 2L-15km-45° (right panel) ET configurations, together with the Vera Rubin Observatory. Vertical dashed lines represent the 68% CI of each distribution, while the black solid lines label the fiducial values.

3.3.2.3 Forecasts for ET. Constraints on deviations from General Relativity and ΛCDM, as those parametrized by the dark energy equation of state and by modified GW propagation, are among the primary targets of the ET science case. Information on these parameters can come from both bright sirens and dark sirens, as we discuss next.

Constraints from bright sirens. Forecasts on the accuracy of the cosmological parameter H_0, Ω_M that can be obtained from bright sirens in the framework of ΛCDM have been presented in section 3.3.1.1. Here, using the same methodology, we enlarge the analysis to modified gravity, extending the analysis performed in [16] — where the inference was carried out on two cosmological parameters at a time — to a more comprehensive investigation. Specifically, this study is conducted on the same dataset of bright sirens (see tables 6 and 10 of [16]), but aims to extract a measurement for all the 6 considered ΛCDM+DE+modified GW propagation parameters H_0, $\Omega_{\mathrm{m},0}$, w_0, w_a, Ξ_0 and n simultaneously. While this choice inevitably leads to broader constraints, we stress that this wider approach is necessary if no other complementary survey's results are readily available to fix one or more parameters in the inference. Furthermore, it represents a standalone benchmark for the additional science that GW astronomy can deliver regardless of the available previous measurements.

We report these results in figures 51, 52 and in table 4, where we also show the impact of using the Planck 2018 [591] posterior distributions as a prior. As expected, extending the analysis to all 6 cosmological parameters worsen the precision on Ξ_0 by a factor of order ~ 5 with respect to the results reported in [16], while n remains undetermined in both cases due to the strong degeneracy with Ξ_0. On the other hand, however, using the early Universe from Planck as priors strongly increase the precision on Ξ_0, which ranges from $\sim 12\%$ in

JCAP03(2026)081

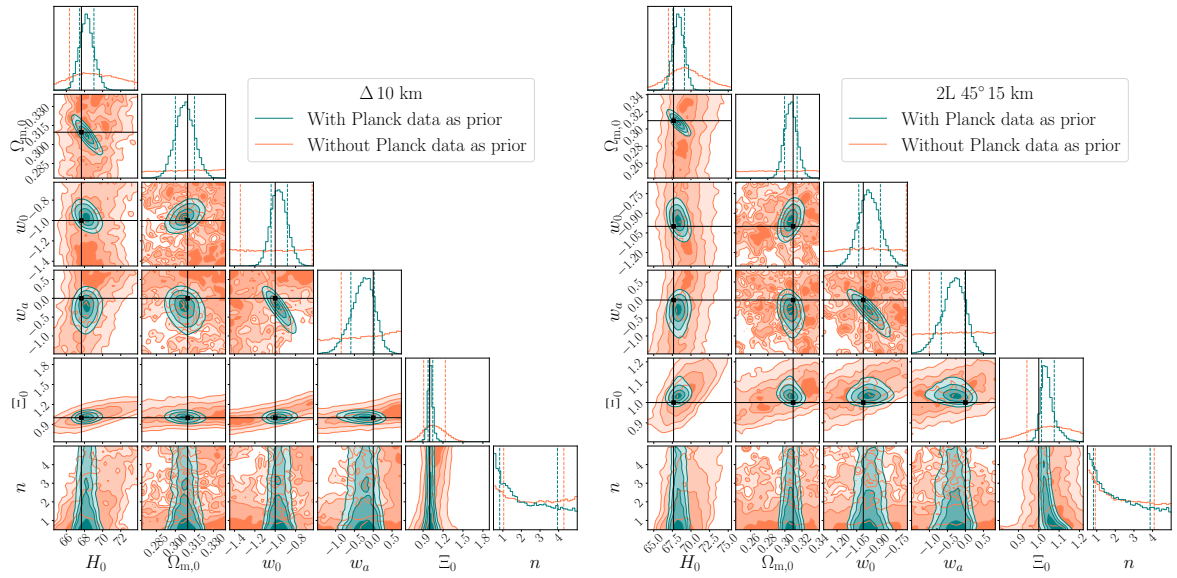

Figure 52. Results of the joint inference on the cosmological parameters H_0, $\Omega_{\mathrm{m},0}$, w_0, w_a, Ξ_0 and n employing GW+GRB events detected in 5 years of observations by the 10 km triangular (left panel) and the 2L-15km-45° (right panel) ET configurations, together with THESEUS. Vertical dashed lines represent the 68% CI of each distribution, while the black solid lines label the fiducial values.

the worst scenario, to $\sim 6\%$ in the best case. The error on H_0, on the other hand, increases only marginally compared to the case when we restrict to ΛCDM. For instance, as we found in section 3.3.1.1, for GW+KN (and 1 yr of observations) in ΛCDM, without using the Planck prior, the relative error on H_0 was 0.9% for the 10-km triangle and 0.6% for 2L-15km misaligned, and these numbers become, respectively, 1.0% and 0.7% when enlarging the parameter space to $\{H_0, \Omega_{\mathrm{m},0}, w_0, w_a, \Xi_0, n\}$. It is also interesting to observe that, as we saw in section 3.3.1.1, in ΛCDM the constraint on H_0 from GW+GRB are much less stringent than from GW+KN. However, we see that this is no longer the case for the Ξ_0 parameter. This is due to the fact that KN observation are restricted to smaller redshifts compared to GRB, while modified GW propagation is a cumulative effect that increases with the distance to the source, and therefore is better probed by high-redshift sources.[26]

Further improvement might come when combining these observations with other distance measurements expected from future standard candles and large-scale structure surveys, in which case the precision on Ξ_0 could reach the $\sim 1\%$ level, while keeping model-independence [1173]. In the context of EFT of dark energy, when identifying Ξ as the effective Planck mass ratio of eq. (3.82), also LSS and CMB data will help constraining Ξ_0 when combined with bright sirens, since in this case the modification in the tensor perturbation sector are related to those in the scalar perturbation sector, and can therfore be constrained also by structure formation data. The price one has to pay is of course to be more model-dependent in order to describe the modifications of gravity in the scalar sector. In the analysis of [1267], it

[26] We also stress again that, as in the discussion in section 3.3.1.1, in this study the relative uncertainty on the luminosity distance has been approximated as 2/SNR, since the Fisher matrix approach breaks down for face on/face off sources. This approximation could be improved in future studies along the lines recently proposed in [1169] and discussed in section 10.2.3.

JCAP03(2026)081

EM Source	ET configuration	Without Planck data priors		With Planck data priors	
		$\Delta\Xi_0/\Xi_0$	Δn	$\Delta\Xi_0/\Xi_0$	Δn
KN	Δ 10 km	0.27	> 1	0.12	> 1
	2L 45° 15 km	0.21	> 1	0.07	> 1
GRB	Δ 10 km	0.31	> 1	0.07	> 1
	2L 45° 15 km	0.27	> 1	0.06	> 1

Table 4. 68% CI relative uncertainties on the modified GW propagation parameters Ξ_0 and n obtained from multimessenger observations and adopting the two shown ET configurations.

was shown that the addition of 500 bright sirens with the triangular 10 km configuration of ET would improve current Planck constraints on Ξ_0 by $\sim 40\%$, for typical late time modifications of gravity where the same Ξ is generating gravitational slip. The further combination with galaxy clustering and weak lensing from an Euclid-like survey would allow reaching an error of 0.3% (more precisely, $\sigma(\Omega_0) = 0.6\%$ with the equivalent parametrization of eq. (3.80)).

Constraints from dark sirens. As we have seen in section 3.3.2.2, the dark siren method based on features on the mass function can provide stringent limits on modified GW propagation. Currently, the best limits are obtained from the BBH mass function, given that the current BNS sample is very small and limited to small redshifts (where the effect of modified GW propagation is suppressed). However, ET will detect a large number of BNS, of order $10^4 - 10^5$ per year, and up to large redshifts of order 2–3. This will allow to use this statistical method also on BNSs, which has the advantage that the BNS mass function is quite narrow, compared to the BBH mass function. The logic behind the possibility of bounding (or observing) modified GW propagation from the BNS mass function can be described as follows [1155]. From a GW detection of a BNS we obtain its GW luminosity distance, $d_L^{\rm gw}$. If Nature is described by a modified gravity theory with $\Xi_0 \neq 1$, $d_L^{\rm gw}$ is different from the electromagnetic luminosity distance $d_L^{\rm em}$; therefore, the source redshift $z_{\rm GR}$ that would be inferred from the measured $d_L^{\rm gw}$ assuming (incorrectly) the validity of GR and ΛCDM, would differ from the true value $z_{\rm true}$. The effect is shown in the left panel of figure 53, for some values of Ξ_0 consistent with the limits given in eqs. (3.83)–(3.85) at about the (1–2)σ level.[27] We see that the effect can become very significant at large redshifts: for instance, if Nature were not described by GR but rather by a modified gravity theory with $\Xi_0 = 1.8$, a source whose true redshift is $z_{\rm true} = 1$, would be assigned a wrong redshift $z_{\rm GR} \simeq 1.45$, if the redshift is inferred assuming $\Xi_0 = 1$.

In turn, this would produce a systematic (and redshift-dependent) bias in the inference of the actual ("source-frame") masses m_i $(i = 1, 2)$ of the component neutron stars, since these are obtained from the measured "detector-frame" masses $m_{({\rm det}),i}$ through the relation $m_i = m_{({\rm det}),i}/(1+z)$. Getting z wrong would then result in a wrong estimate of m_i. More

[27] In this plot, we use for illustration the same values of H_0 and Ω_M in the modified gravity theory and in GR, setting them to $H_0 = 67.9\,{\rm km/(s\,Mpc)}$ and $\Omega_M = 0.30$. In a full analysis, all cosmological parameters will have to be determined self-consistently in GR and in modified gravity, by fitting the prediction of each theory to the cosmological observations.

JCAP03(2026)081

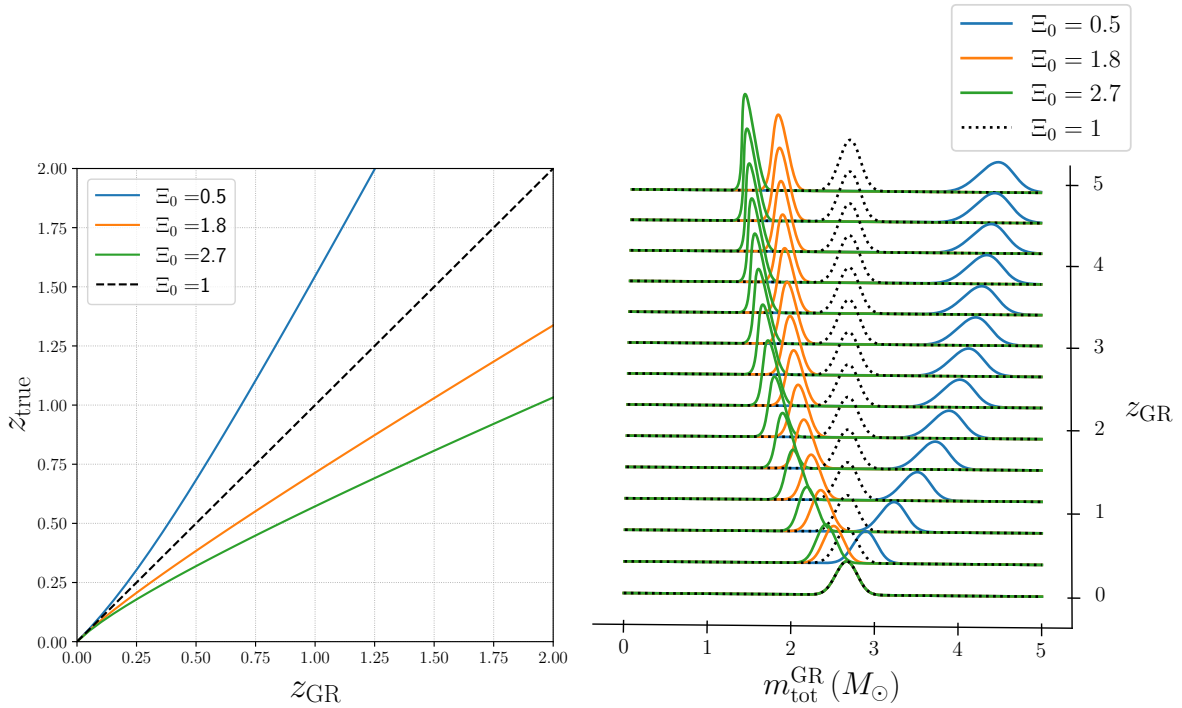

Figure 53. *Left:* the redshift $z_{\rm true}$ of a source, as a function of the value $z_{\rm GR}$ that would be incorrectly inferred using GR if Nature is described by a modified gravity theory with $\Xi_0 \neq 1$, for different values of Ξ_0. *Right:* the effect on the distribution of the total mass of the binary from a 'wrong' reconstruction using GR, $m_{\rm tot}^{\rm GR}$, assuming that the true distribution of the source-frame total mass of the binary is a (redshift-independent) Gaussian, with mean $2.66M_\odot$ and standard deviation $0.13M_\odot$. Adapted from [1155]. Reproduced from [1155]. CC BY 4.0.

precisely, if Nature is described by a modified gravity theory with $\Xi_0 \neq 1$, the true values of the source-frame masses, $m_{{\rm true},i}$ are obtained from the observed detector-frame masses by $m_{{\rm true},i} = m_{({\rm det}),i}/(1+z_{\rm true})$, while the values incorrectly inferred assuming GR would be $m_{{\rm GR},i} = m_{({\rm det}),i}/(1+z_{\rm GR})$, and therefore

$$m_{{\rm true},i} = \left(\frac{1+z_{\rm GR}}{1+z_{\rm true}}\right) m_{{\rm GR},i}\,. \tag{3.86}$$

For instance (assuming again, as an example, $\Xi_0 = 1.8$), for a NS with $m_{\rm true} = 1.35M_\odot$ at $z_{\rm true} = 1$, the mass incorrectly inferred from GR would be $m_{\rm GR} \simeq 1.10M_\odot$, while for $z_{\rm true} = 2$, in GR one would infer $m_{\rm GR} \simeq 0.99M_\odot$. The effect is quite striking because it would bias, in the same way, all NS masses at a given z (so, in particular, both masses of a BNS, contrary to what could be expected from evolutionary paths leading to accretion of matter on one of the two neutron stars), shifting the whole distribution of NS masses in a characteristic redshift-dependent manner. This is shown (for the distribution of the total mass of the binary) in the right panel of figure 53.

Given the large number of BNS that ET will detect, this method can in principle reach a very good accuracy on Ξ_0. The effect can be tested directly on the chirp mass of the system, which is very accurately measured, so in the end, with this technique, the main error on $d_L^{\rm gw}/d_L^{\rm em}$ from a single BNS is expected to be of order of the relative width of the BNS mass

JCAP03(2026)081

function. With N detections at sufficiently large redshift, where the effect of modified GW propagation can be sizable, the error scale approximately as $1/\sqrt{N}$, so sub-percent errors on Ξ_0 could be obtained, as long as other competing sources of biases, such as lensing or a possible redshift evolution of the BNS mass function [1276], can be adequately accounted for.

3.3.3 GW lensing

According to GR, if a GW encounters a massive object on its travel path from source to observer, it can undergo gravitational lensing. Depending on the lens mass and the lens-source alignment, one can get different effects; for the lowest masses and more misaligned systems, one has microlensing, where the GW undergoes frequency-dependent modulations [101, 1277]. On the other hand, for more massive lenses and better-aligned systems, one is in the geometric optics regime, and the wave is split into multiple copies of the original system, with an overall magnification, and overall phase shift and a time delay [101, 1278]. If the system is less aligned and/or the lens lighter, the various images have a small time delay and overlap, leading to a single non-trivial signal in the detector, called millilensing [1279]. For larger masses, the images are individually resolvable, generally referred to as strong lensing [1278]. While rates for micro and millilensing are uncertain — due to their strong dependency on the nature of dark matter— strong lensing is expected to be already observable for BBH signals in current detectors [106, 1280]. Hundreds of such lensed signals [107] and tens of lensed BNSs should be observed in next-generation detectors every year [1281]. A fraction of the latter could also have an observable lensed EM counterpart, making their correlation easier to do [1282].

3.3.3.1 GW lensing as probe of cosmological parameters. In the geometric optics, according to GR, GW and light are bend the same way, which can be leveraged to study our Universe, with unique possibilities at high redshift. Indeed, if a GW coming from a BBH is lensed, then the EM emission from its host galaxy is also lensed. One can then match both to use their complementary information to probe various physical phenomena [1283, 1284]. Matching a lensed BBH and its host galaxy is also easier than for an unlensed signal because lensing offers a much more precise sky localization [103]. In addition, GW measurements lead to millisecond precision measurements of the arrival times, and one can use time delay cosmography to constrain cosmological parameters [1285], provided the EM observations complete the observations by giving access to the lens and source redshifts. Moreover, one can also have extra constraints via the reconstructed magnifications of the images. The total measure obtained for the Hubble constant is relatively accurate, even for a single observation [1283]. Additionally, in next-generation detectors, several observations can be stacked to improve the final constraints, similarly to what is already done nowadays for dark sirens [9]. When the BBH host galaxy cannot be identified, one can still develop a dark sirens-like approach for lensing, which accounts for a list of possible counterparts and the probability to miss the genuine system in the EM. While less precise than with a direct access to the counterpart in the EM, the list of candidates will be more restrained than for the usual dark siren method thanks to the selection done using the observed lens characteristics [1283]. Moreover, these events would also allow for measurements at higher redshifts than unlensed systems, giving extra insights on the early Universe.

JCAP03(2026)081

Furthermore, lensed events without EM counterpart can be used to constraint cosmology based on their statistical properties, using the fact that the expected number of lensed events and the distribution of the time delay between lensed images depend on the cosmology. In particular, in ref. [1286] is shown how the expected distributions of lensed GW events can be used to constrain the cosmological parameters. Denoting by N the number of lensed BBHs events observed over an extended period of time $T_{\rm obs}$ (each one assumed to produce two copies of the observed GW signal), and by $\{\Delta t_i\}, i = 1, \ldots, N$ their corresponding time delays, one can construct a probability distribution for the cosmological parameters $\vec{\Omega}$ as

$$p(\vec{\Omega}|N, \{\Delta t_i\}, T_{\rm obs}) = \frac{p(\vec{\Omega}) p(N|\vec{\Omega}, T_{\rm obs}) p(\{\Delta t_i\}|\vec{\Omega}, T_{\rm obs})}{Z}, \tag{3.87}$$

where one uses the conditional independency between the time delays and the number of lensed BBH detections given the parameters and the observation time $T_{\rm obs}$; $p(\vec{\Omega})$ is the prior and Z is the normalization constant. By performing various simulations on a coarse grid of values for the cosmological parameters, it is then possible to construct the two probability functions. Then, one can evaluate those with a given observation time and find a probability distribution for the cosmological parameters. With this approach, using 10 years of observation and a BBH merger rate of $5 \times 10^5\,{\rm yr}^{-1}$ with 3G detectors (made of CE and ET), one obtains $H_0 = 67.8 \pm 1.1\,{\rm km\,s^{-1}Mpc^{-1}}$ and $\Omega_m = 0.3142 \pm 0.0056$ at 1-σ C.I. for the standard ΛCDM cosmology. Figure 54 shows the posterior distribution for the cosmological parameters found with this methods. The bounds obtained depend on the detection rate, with broader constraints for lower rates. Besides, the approach also works for other cosmological models, such as wCDM, where the same observational conditions lead to competitive bounds compared to other traditional approaches (see right plot in figure 54) [1286]. An interesting feature of these observations is that (a fraction of) such BBHs can come from high redshift, and, therefore, such studies could also probe cosmological parameters in a regime that is not explored by other methods.

As discussed in section 3.3.2, modified GW propagation can be a smoking gun for modifications of gravity at cosmological scales, and lensing can also be used to study it [1287, 1288]. Basically, if one observes a strongly lensed GW and its EM counterpart, and performs the lens reconstruction, one can access two different measures of the luminosity distance: one via GWs — by correcting the measured luminosity distance by the magnification, and one by the EM redshift measurements. If GR is the correct theory of gravity, the two values should match. However, in the presence of modified GW propagation, the two quantities will be different, and the difference can be used to constrain the parameter(s) linking the two quantities. This can be done for the Ξ_0 parametrization mentioned above [1287] but also for other theories such as large extra spatial dimensions or a time-varying Planck mass [1288]. This method can be used for lensed BNS, NSBH, and BBH events. The former have the advantage of offering a better sky location thanks to the use of Earth rotation in addition to the multiple images [1289], while the latter would lead to better constraints thanks to the fact that, for a given SNR, they can be detected to larger distance.

Another way to look into possible modifications in long-distance propagation is to test the speed of gravity by comparing the arrival time of photons and GWs [3]. For unlensed events, the intrinsic difference in emission time between photons and GWs is one of the main

JCAP03(2026)081

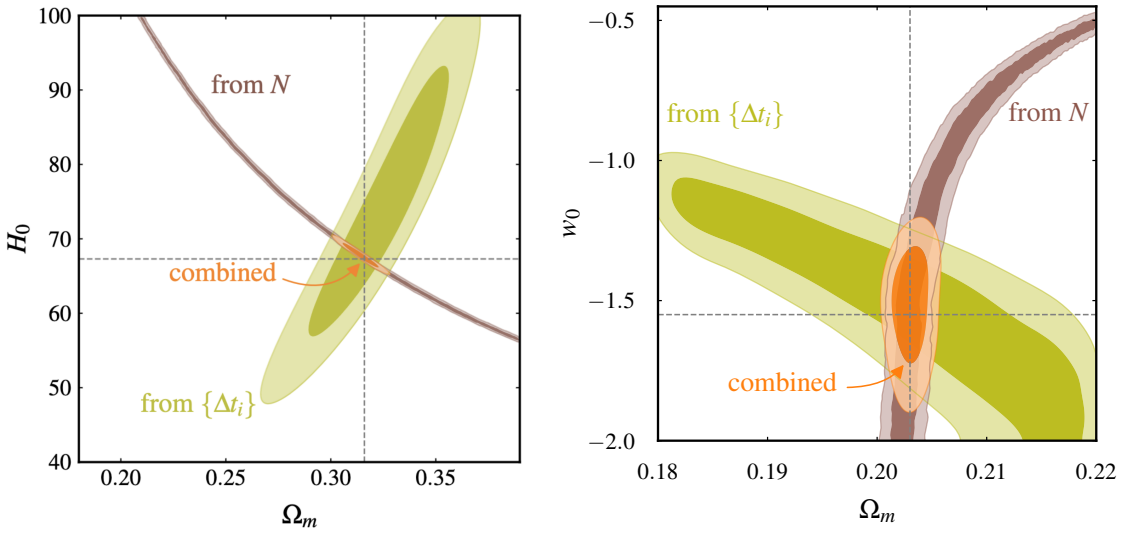

Figure 54. Constraints obtained from the statistical method relying on lensed BBH events to constrain the cosmological parameters presented in [1286]. *Left:* H_0 vs. Ω_m. *Right:* w_0 vs. Ω_m. These results are obtained for a ten year observation period, assuming that a generic network of 3G detectors will have a nominal BBH detection rate of $5 \times 10^5\,\mathrm{yr}^{-1}$ upto a typical redshift of $z_{\max} \sim 15$ (exact value dependent on the cosmology and population models), and that their time of arrivals will be measured precisely. The bounds obtained are competitive with other studies, and the BBH signals originate from further away, potentially carrying information from earlier periods in the Universe. Figures adapted from [1286]. Reprinted figure with permission from [1286], Copyright (2023) by the American Physical Society.

sources of uncertainty, and varies from one model to the other [3]. As mentioned above, if a GW is lensed, the light emitted by its source is also lensed. Therefore, we would now have multiple measures of the difference in arrival time between GW and EM. Moreover, by comparing the differences between EM and GW measured for the various images, one can cancel out several nuisance terms in the measure, and in particular the intrinsic difference in emission time [1290, 1291]. Therefore, one may expect a more precise measurement of the speed of gravity, depending on the source of EM emission. Also, this method suffers from different sources of uncertainties (related to the lens itself and not the time of emission), so it can be used to cross-check the measurements made with other observations.

3.3.3.2 GW lensing and dark matter. When a GW is lensed, the lensing effect encodes the mass and density profile of the lens. Therefore, it can be used to probe the lens itself. In particular, millilensing and microlensing originate from smaller-scale objects, which can potentially match some dark matter candidates such as dark matter halos or primordial black holes. A particularly interesting case is when one searches for micro- or millilensing effects on top of strong lensing; if a GW is deflected by a galaxy or a galaxy cluster, one image or more can interact with smaller objects in the macrolens. These can be stars or dark matter [1292–1294]. In particular, relying on different mass models, and looking how the mass is distributed in the lens, it is possible to probe various dark matter models [1295]. The same is true for millilensing, where objects are heavier than for microlensing, corresponding

JCAP03(2026)081

to the expected mass regime of dark matter halos. However, the number of images, their magnifications and time delays inform us about the objects within the galaxy that lead to the extra effect [1279]. Knowing more about the scale helps constraining dark matter models since, from one model to the other, different scales are favored or prohibited [1296, 1297]. Alternatively, isolated objects can also lead to such lensing effects, and they can be used to study the abundance of intermediate-mass and primordial black holes [1298, 1299]. For these studies, micro- and milli-lensing effects from baryonic substructures need to be carefully accounted for. Effects similar to microlensing can stem from other sources, such as orbital precession, missing waveform features or noise artefacts. Recent and ongoing work attempt to break the degeneracies in order to distinguish true microlensing from such false positives [1300–1302]. For micro- and millilensing searches, ET offers the interesting advantage of enabling the detection of more subtle features thanks to its enhanced sensitivity.

The above assumes the detection of micro or millilensing. However, non-detection can also be particularly useful to constrain the fraction of dark matter made of compact objects such as MACHO's [1303]. Indeed, depending on the model for dark matter, the fraction of it made of compact objects, and the BBH distribution, one can expect a different number of detected microlensed events. So, in the absence of detection, one can constrain the dark matter fraction made of compact objects. This is done by simulating many realisations with different fractions and checking which ones are compatible with the non-observation, leading to an upper bound on this fraction [1303, 1304]. If a microlensed GW is detected, it is also possible to use this to put a lower bound on the dark matter fraction. For this, ET offers extra opportunities thanks to its additional sensitivity within the volume already probed, but also thanks to its larger horizon distance, increasing the probability for lensing.

3.3.3.3 Impact of lensing on standard sirens measurements. In the previous paragraphs we have discussed the prospects of lensing as an extra source of information. On the other hand, it is important to highlight that lensing can also act as an additional source of nuisance or systematic uncertainty in standard siren measurements. Besides unrecognized strongly lensed events, the phenomenon of weak lensing due to the gravitational potential of large-scale structures in the Universe is ubiquitous, as it accumulates along the propagating paths of all GWs [1139, 1305–1307]. Within the geometric optics approximation, lensing induces frequency-independent (de)magnification of the GW amplitude, which directly translates to the inference of a biased luminosity distance of the GW source:

$$d_{\rm L}^{\rm obs}(z,\mu) = \frac{d_{\rm L}^{\rm true}(z)}{\sqrt{\mu}} \,, \tag{3.88}$$

where $d_{\rm L}^{\rm true}$ is the true luminosity distance of the GW source and μ is the lensing magnification. The probability distribution function of the lensing magnification depends on the redshift of the source; it is sharply peaked at $\mu \approx 1$ [1308], such that the majority of events will suffer very small modification, but it has a tail towards high magnifications that becomes more relevant for increasing redshifts. Moreover, lensing selection effects, i.e. the fact that magnified events are more likely to be detected than demagnified ones, tend to worsen its impact [1309–1311]. This effect is usually accounted as an additional source of noise in the luminosity distance uncertainty [1312], worsening the estimation of the cosmological parameters, particularly

JCAP03(2026)081

those relying on distant events. Focusing on the case of bright standard sirens, lensing can also act as a systematic uncertainty in the estimation of such cosmological parameters. Using idealized mock catalogs of bright standard sirens events, relevant for ET, [1308] shows that in some scenarios the lensing bias on the cosmological parameters can be comparable or greater than the expected statistical uncertainty. In this regard, [1313] highlights the importance of properly modeling the lensing magnification probability distribution function when evaluating the expected lensing uncertainty. Furthermore, in the absence of an EM counterpart, and when the mass-redshift degeneracy cannot be broken by any other external information, lensing can also impact the inference of the source-frame masses of the GW sources [1282, 1314–1316]. In particular, in the case of BNS mergers, the masses can be magnified above the intrinsic maximum mass of the distribution, thus falling into the lower mass gap. In the era of ET, it would be important to account for this effect, to properly infer the maximum mass of NSs and to avoid misinterpretation of NS events as BH ones, spoiling for example the multi-messenger searches. In the coming years, the development of mitigation strategies in the data analysis will be necessary to properly account for lensing in ET events.

3.4 Probing the large scale structure of the Universe

3.4.1 Cross-correlation GWxLSS

As a cosmic tracer of the underlying matter distribution, resolved GWs and the GWB offer the unique possibility to map the large scale structure (LSS) of the Universe though gravitational radiation [547, 1317, 1318]. In the ET era, the anisotropic distribution of GWs will provide an independent cosmological probe and effectively become a useful LSS tracers in a complementary way to other LSS surveys (that trace cosmic structures through redshift measurements), as well as to emerging techniques such as Line Intensity Mapping or HI intensity mapping. Since all those map the same underlying density field via complementary observables, their cross-correlation offers a new opportunity for Cosmology and probing modified gravity (see also [1317, 1319–1327]).

3.4.1.1 Cross-correlation of GW resolved events with LSS. Besides information that can be extracted from individual detections (such as in the case of bright sirens) or from ensemble of GW detections (such as from dark sirens), large GW catalogs of resolved events open more general possibilities. They naturally trace structure in a luminosity distance space [1318], whereas galaxy surveys probe the redshift space [1328]. The expected number count exhibits different effects in both spaces, and the mapping of one into the other depend on both cosmology and gravity theory. The expression for the relativistic number count in luminosity distance space was initially considered in [1329] (see [1174, 1318] for subsequent studies), and then calculated in full generality in [1307, 1330]. Importantly, these works showed that the result is different with respect to its analogue in redshift space, with contributions such as lensing including additional terms. Those differences will become relevant for ET, which could allow using tomographic redshift bins up to $z \sim 2$ [1307]. Ref. [1331] further models the evolution and magnification biases for 3G detectors which affect those contributions.

Interestingly, similarly to supernovae, bright sirens are useful tracers not only of the density but also of the velocity field [1332, 1333], because the latter introduces correlations in

JCAP03(2026)081

the distances which are well modelled by linear theory [1334]. Combining both measurements, one can improve precision substantially by breaking the degeneracy between fundamental parameters such as σ_8 and the tracer bias. Moreover, combining with a galaxy catalog covering the same area of the sky, one gains access to a total of one velocity and two density tracers. One can thus probe six power spectra with the different combinations, and perform a 6×2pt analysis [1174, 1335]. In particular, it was shown in [1174] that, using GW signals from BNS with ET with kilonova follow-ups from the Vera Rubin Observatory,[28] together with DESI galaxies[29] in the range $0 < z < 0.5$, such an analysis could, when compared to a standard BNS Hubble diagram one, improve H_0 precision by 30%, improve precision in Ω_{k0} by a factor of more than 10 (reaching $\sigma(\Omega_{k0}) < 0.02$ in 5 years), and constrain well both σ_8 and the growth-rate index simultaneously. Therefore, a joint analysis of GWs and LSS will help address both H_0 and σ_8 tensions. Figure 55 shows forecasts obtained in [1174] for BNS with KN obtained with a Vera Rubin Observatory follow-up, together with DESI BGS galaxies in an area of $14000\,\mathrm{deg}^2$, assuming a maximum wavenumber $k_{\rm max} = 0.1\,h/\mathrm{Mpc}$ and $z_{\rm max} = 0.5$. The forecast is for $\{\sigma_8, \gamma, \Omega_{m0}, \Omega_{k0}, H_0\}$, where γ is the growth-rate index, which is assumed constant as a simple parametrization of beyond-GR gravity, marginalized over two free bias parameters in each of 5 redshift bins and three global non-linear redshift-space distortion parameters.

Basic formalism. The anisotropic distribution of resolved GW events is described by the relative GW number count fluctuation in a direction $\mathbf{n}$ and at redshift z defined as

$$\Delta(\mathbf{n}, z) = \frac{N - \langle N \rangle}{\langle N \rangle}. \tag{3.89}$$

Given that GW interferometes are effectively all-sky experiments, it is convenient to study the n-point functions of this stochastic field in a base that reflects the intrinsic symmetry of the sky. Therefore, following the treatment presented in [1320], we decompose the number count fluctuation in a spherical harmonics base and we study the angular power spectrum given by

$$C_\ell^{XY}(z_i, z_j) = \frac{2}{\pi} \int \frac{dk}{k} \mathcal{P}(k) \Delta^{X,z_i}(k) \Delta^{Y,z_j}(k)\,, \tag{3.90}$$

where we allow for the possibility of including different tracers X, Y (GWs and/or galaxies) in different redshift bins, and $\mathcal{P}(k)$ is the (almost-scale invariant) primordial scalar power spectrum. The number count fluctuation $\Delta^{X,z_i}(k)$ reads as

$$\Delta^{X,z_i}(k) = \int_0^\infty dz \frac{dN_X}{dz} w(z, z_i) \Delta^X(k, z), \tag{3.91}$$

where dN_X/dz is the *observed* source number density per redshift interval, $w(z, z_i)$ a normalized window function centered at redshift z_i, and $\Delta^X(k, z)$ encodes contributions from density, velocity, lensing and gravity effects [552, 1328].

[28] https://www.lsst.org/.
[29] https://www.desi.lbl.gov/.

JCAP03(2026)081

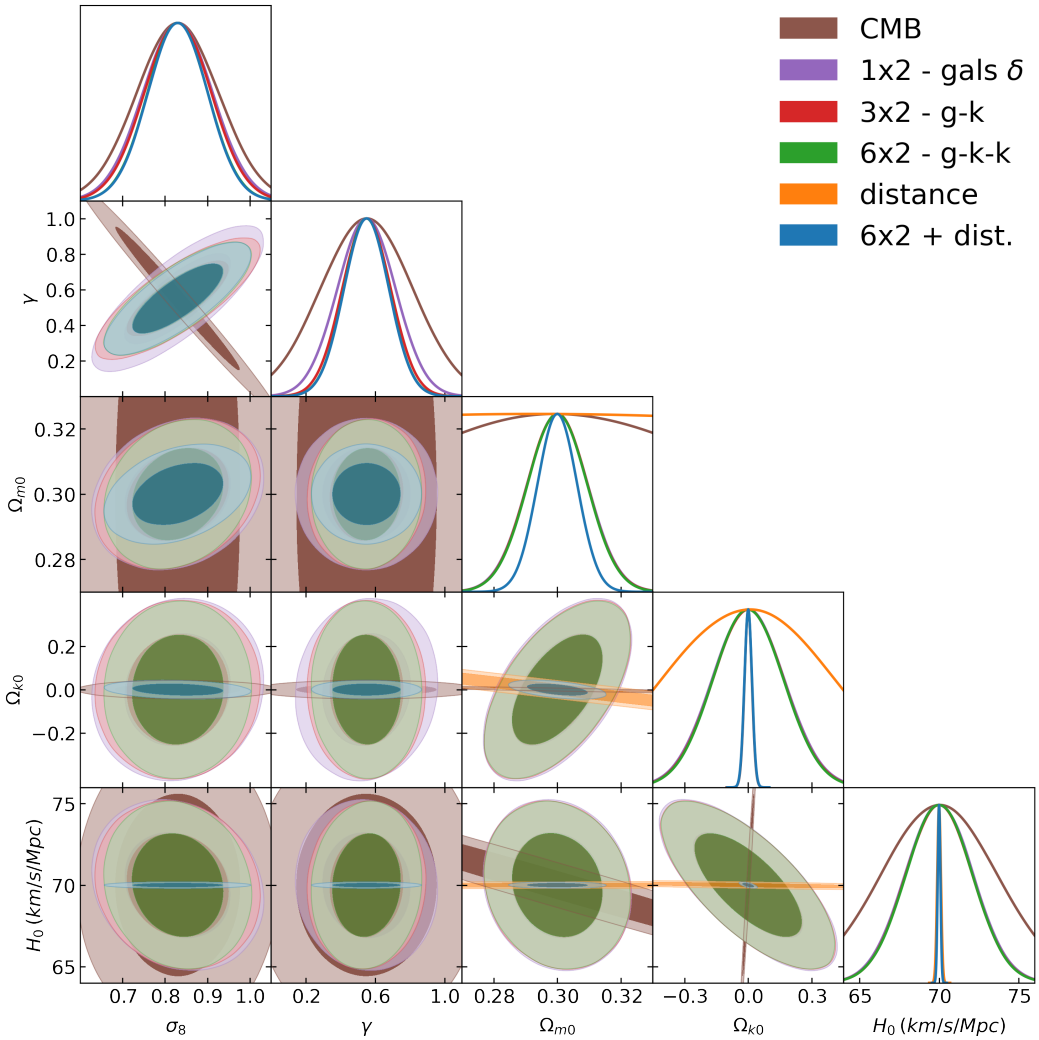

Figure 55. Marginalised constraints (1σ and 2σ confidence regions) combining ET KN and galaxies for $z \leq 0.5$, separated according to the method used. Purple: only DESI BGS galaxies; Red: DESI+KN velocities (3×2pt); Green: DESI+KN in the full 6×2pt; Orange: KN distances only; Blue: 6×2pt + distances; Brown: CMB. Reproduced with permission from [1174].

Noise, dependence on the population model and detector sensitivity. Since GWs are a discrete tracer of the LSS, their angular power spectrum measurement has a shot noise contribution analogous, for instance, to that of galaxies. Assuming the noise of different experiments and in different redshift bins to be uncorrelated, the shot noise reads as $\mathcal{N}_\ell^{XY} = \delta_{XY}\delta_{ij}(dN_X/d\Omega)^{-1}$, where $dN_X(z_i)/d\Omega$ is the *total* number of *observed* sources per steradian in the i-th redshift bin. This quantity depends on the population properties, in particular on the total merger rate and on detector sensitivity. Conversely, we note that the signal in eq. (3.91) depends on a normalized window function, hence the dependence on the population model is through its shape rather than through its overall amplitude [1320].

For GW sources, an important difference with LSS studies is the limited angular resolution of GW detectors. The best angular resolution determines a limiting scale in the angular

JCAP03(2026)081

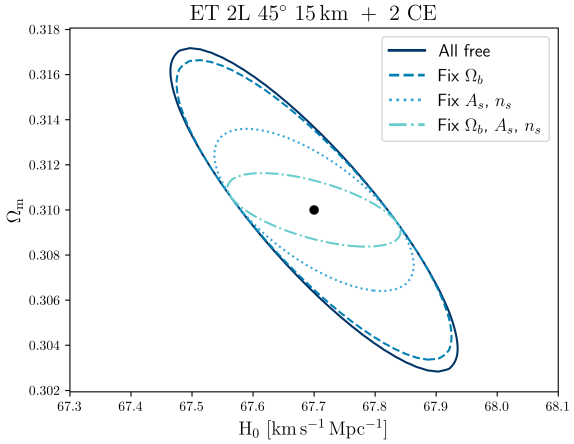

Parameter	All nuisance parameters free	Fix Ω_b	Fix A_s, n_s	Fix Ω_b, A_s, n_s
ET 2L 45° 15 km + 2CE				
H_0	0.8	0.75	0.55	0.47
Ω_m	5.3	4.9	2.6	1.2
ET Δ 10 km + 2CE				
H_0	0.8	0.79	0.6	0.53
Ω_m	5.3	4.9	2.6	1.2

Figure 56. *Left:* 1σ constraints in the $H_0 - \Omega_\mathrm{m}$ plane from the tomographic angular auto- and cross-correlation of resolved BBHs with a Euclid-like photometric galaxy catalog, for ET in the 2L configuration in combination with two CE detectors. Different lines correspond to fixing other cosmological parameters (baryon density Ω_b, amplitude A_s and spectral index n_s of the primordial power spectrum), representing the case where prior knowledge is assumed on those, while still marginalising over the tracers' bias. The case of a triangular ET is not displayed since almost indistinguishable. *Right:* relative errors (in %) on H_0, Ω_m for the 2L and triangular configurations of ET. Results from [1338]. Reproduced from [1338]. CC BY 4.0.

power spectrum [1318, 1319, 1323, 1324], $\ell_\mathrm{max} \sim 180°/\Delta\Omega_\mathrm{max}^{1/2}$ with $\Delta\Omega_\mathrm{max}$ being the best 1σ sky localization of the GW catalog. From figure 47, we see that the best angular resolution of ET alone corresponds to roughly $\Delta\Omega_\mathrm{max} \sim 0.1\,\mathrm{deg}^2$, hence a maximum multipole of at most ~ 300 in a local redshift shell (up to $z \sim 0.2$), while for higher redshifts the range will be further limited. The effect of limited spatial resolution can be effectively modeled as a smoothing of the underlying overdensity field by an observational "beam", similarly to CMB experiments. A common choice in the literature is to parametrize this effect with a Gaussian beam, inducing an exponential damping in the GW-GW correlation signal [1318, 1323, 1324, 1336]. Moreover, error in distance/redshift localization can be accounted as showed in refs. [1318, 1319, 1324, 1336], which suggested to implement a probabilistic treatment similar to those employed in weak lensing analysis, where photometric redshifts carry a non-negligible uncertainty.

Cosmography. In presence of tracers of the same density fields in distance and redshift spaces, the cross-correlation signal depends on the parameters of the distance-redshift relation. Here we consider in particular GW sources correlated with a galaxy catalog, as well as the respective auto-correlations. The window function in eq. (3.91) takes the schematic form $w_i(z|\text{bin in } z)$ for the galaxy survey and $w_i(d_L(z, H_0, \ldots)|\text{bin in } d_L)$ for the GW catalog. That is, the binning is performed in the spaces where sources are observed — redshift for galaxies and luminosity distance for GWs, but GW sources distributed according to the source-frame distribution $dN_\mathrm{GW}(z_i)/dz$ are observed in different distance bins depending on the value of the parameters determining the distance-redshift relation, with the likelihood of the observed signal being maximised for the correct cosmology [1319, 1337, 1338].

JCAP03(2026)081

Figure 56 shows the forecasts in the $H_0 - \Omega_{\rm m}$ plane obtained in [1338] for the auto- and cross-angular power spectrum in tomographic redshift/distance bins [see eq. (3.90)] of GW sources with a galaxy catalog with the specifics of the Euclid photometric survey [1210, 1339]. While the application of this technique to ET alone is possible, the angular resolution highly benefits from the presence of a network of detectors. So, we focus on 10 years of observations of ET in combination with two CE detectors. We refer to [16] for a description of the BBH population used. We employ a Fisher matrix analysis with 20 equally populated redshift bins for the galaxy catalog, converted into luminosity distance bins for GW events assuming a fiducial cosmology. We account for the dominant contributions to the number count fluctuation, namely density and lensing [1307]. We also include the effect of the limited angular resolution with an exponential damping in the signal, with a redshift dependence computed in each redshift bin from the median localization in the simulations shown in figure 47. Furthermore, we restrict to a maximum multipole $\ell_{\rm max} = 300$ in any case, and for GW sources we impose a stricter hard cut on the maximum multipole in each bin (denoted with the index i) at $\ell_{\rm max,i} = \pi/\sqrt{\Delta\Omega_{\rm min,i}}$ being $\Delta\Omega_{\rm min,i}$ the best sky localization in the bin. The result is marginalised over the amplitude and spectral index of the primordial power spectrum, the baryon density, and the amplitude of the GW and galaxy bias in each bin, for a total of 43 nuisance parameters. Therefore, importantly in light of the Hubble tension, this constraints are independent on any other external probe or prior (e.g. BBN, CMB, SNe). We also show the result obtained fixing the baryon density Ω_b and primordial power spectrum amplitude A_s and spectral index n_s to their fiducial values, corresponding to the case where external priors are added. The relative error is reported in the table in the right panel of figure 56. In the best case, we forecast a 0.8% measurement of H_0, which can be reduced to $\sim 0.5\%$ when assuming prior knowledge of Ω_b, A_s, n_s, in which case a $\sim 1\%$ measurement of Ω_m is also obtained. In conclusion, the cross-correlation technique for ET in combination with CE can lead to a promising sub-percent determination of H_0, with percent-level precision already reached after one year of operation.

Reconstructing the Hubble diagram from cross-correlations of GW sources and tracers in redshift space can also be done directly through full-sky cosmological galaxy mock simulations. In [1340], the authors employ thousands of relativistic galaxy simulations together with binary black-hole sky maps populating the same large-scale structures of the galaxy maps, taking into account various systematic sources of anisotropies: the direction dependent sensitivities of both 2G and 3G GW networks, galaxy mask, the lensing magnification of luminosity distances, and modeling BBHs as extended sources due to the much larger errors in the determination of their 3D positions (RA, Dec, D_L) as compared to the ones for galaxies. Ref. [1340] shows that the method is robust to all these effects and to the choice of fiducial cosmology behind the simulations. This means that the position of the crest in the (z, D_L) plane illustrated in figure 57 is a cosmic standard ruler, not depending strongly on the details of the individual large-scale structures in the two spaces (distance or redshift) and rather on their matching. With such technique, one can get sub-percent measurements of the Hubble constant with 5 years of ET+2CE, while measuring also other cosmological parameters, which is one order of magnitude more precise than what is expected from the next observing run of LVK (O5). Moreover, if LVK is still active at the time of ET, LVK would help ET on

JCAP03(2026)081

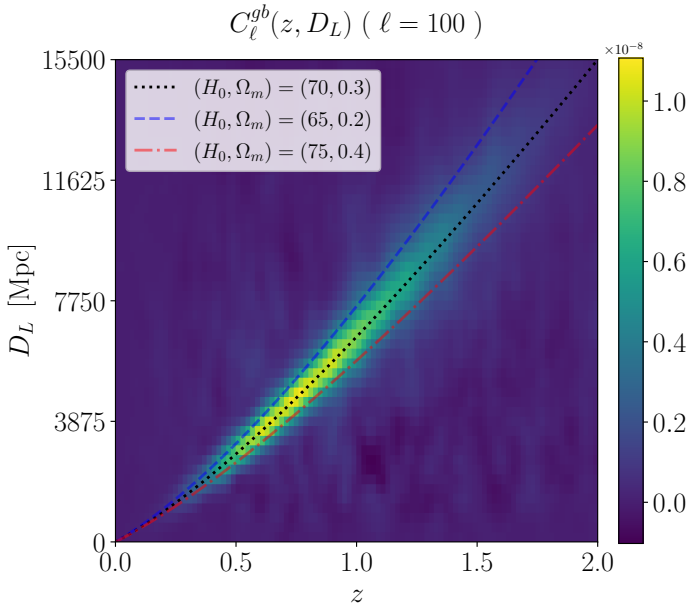

Figure 57. The cross-correlation between the harmonic modes of galaxies (g) at z and BBHs (b) at D_L leads to a cross-angular power spectrum $C_\ell^{gb}(z, D_L)$. We show the average cross-spectrum for 1000 light-cone simulations of galaxies and BBHs, for $\ell = 100$ ($\sim 2°$). When a shell in z coincides with a shell in D_L, the correlation between the galaxy and BBH maps is maximal. The red, blue and black lines correspond to the Hubble diagrams $D_L(z)$ of three different cosmologies — in the fiducial model $H_0 = 70.0\,\mathrm{km\,s^{-1}\,Mpc^{-1}}$ and $\Omega_m = 0.3$. Reproduced from [1340],

localizing binary sources, even when those are below the detection thresholds for the 2G network, also potentially leading to sub-percent level measurements of H_0.

Modified gravity. One of the goals of all next generation cosmological experiments is to test General Relativity in the late Universe. In particular, General Relativity has not been fully tested on scales comparable to today's cosmological horizon. At those scales projection effects have the largest impact on the clustering of LSS tracers, while, at the same time, being very sensitive to deviations from General Relativity. Therefore GW clustering offer the unique possibility to fulfill this task in a complementary fashion to galaxy surveys or line intensity mapping experiments.

Two possible extensions that can be tested are: an equation of state for dark energy $w_{\rm DE} \neq -1$, and a modified growth of structure, often parametrised via the (possibly) time- and scale-dependent μ, η functions defined as [1341]

$$k^2\Psi(k,z) = -4\pi G a^2 \mu(k,z)\bar{\rho}D, \qquad \Phi(k,z) = \eta(k,z)\Psi(k,z), \tag{3.92}$$

where Ψ, Φ are the Bardeen potentials, a is the scale factor, $\bar{\rho}$ is the background energy density, and D is the gauge-invariant energy density fluctuation. This parametrization allows to test a broad class of models, from scalar-tensor theories [1342–1345] to models that invoke extra dimensions [1346], by choosing an appropriate time- and scale-dependence of the μ, η variables.

JCAP03(2026)081

Many different authors employed different parametrisations to forecast sensitivity of next generation GW observatory, such as ET, on deviations from General Relativity, both as unique probe or by cross-correlating this datasets with galaxy clustering, weak lensing and HI line intensity mapping [1323, 1324, 1347]. Constraints on these parameters are heavily dependent on the chosen parametrization, however the general consensus is that in all the cases ET alone, or in synergy with Cosmic Explorer, will provide unparalleled constraints on extensions of General Relativity.

Primordial black holes. The clustering properties of PBH binaries can be substantially different from those of traditional stellar-origin BH binaries [1325, 1348, 1349]. While astrophysical BH binaries are the result of intense stellar formation history in galaxies, and thus they trace the galaxy (anisotropic) spatial distribution, PBH binaries trace a different kind of environment, depending on their formation channel (see section 4 for detailed discussion). In particular, there are two well-understood formation channels that are worth mentioning: early-time [1350] and late-time binaries [1348, 1351]. In the former channel, binaries start forming in the early Universe, during radiation domination, and therefore they are thought to evenly trace all sort of dark matter structure that form in the late Universe. In the latter formation channel, binaries are expected to form in the late Universe in low-mass dark matter halos ($M_{\rm halo} \simeq 10^2 - 10^3\ M_\odot$) via a direct capture process because of the low relative velocity of halo particles.

Clustering properties of GWs depend mainly on the bias parameter $b_{\rm GW}$. Since astrophysical binaries trace luminous galaxy distributions, we expect them to have a bias close to that of galaxies, i.e., $b_{\rm GW} \sim b_{\rm gal} \sim 1.2 - 3.0$. On the other hand, early-time binaries, since they effectively trace the entire dark matter distribution, are expected to have $b_{\rm GW} \sim 1$. Finally, late-time binaries, because of the peculiarity of their formation mechanism, trace only low mass halos, mostly in filaments, thus they have $b_{\rm GW} \sim 0.5$. Therefore, it is possible to disentangle PBHs from astrophysical binaries by measuring the GW bias with sufficient precision. Even in this case, the exact numbers depend on the modeling of PBHs; however the consensus reached by different studies is that by measuring the bias with a precision of order few percent it is possible to constraint PBH abundance at the ten percent level [1320, 1324, 1325, 1347, 1349]. Interestingly, reaching that level of precision will be well within the reach of ET in combination with many current and future LSS surveys, making it potentially capable of resolving the long-standing issue of what the nature of dark matter is [1325].

3.4.1.2 Cross-correlation of AGWB with LSS. In section 3.1.2.2 it has been discussed that the inhomogeneous distribution of sources and the line-of-sight effects accumulated during propagation contribute to the anisotropies of the AGWB. These intrinsic anisotropies are generated by the primordial perturbations in the Universe on large angular scales, and therefore constitute a tracer of the LSS. This implies that the cross-correlation of the anisotropies of the AGWB with other tracers of the LSS, such as galaxy number counts [546, 549, 557, 589, 1352, 1353], weak gravitational lensing [546, 549], CMB [578], and CMB lensing [1354], could be very large in light of the common seeds of the perturbations which generate the anisotropies of these signals.

JCAP03(2026)081

It is possible indeed to characterize the anisotropies of the AGWB as a tracer of the LSS by computing the redshift distribution, the bias, and the magnification bias of the AGWB energy density, as shown in [547, 551, 552]. Among these three functions, the bias is of particular interest, since it contains information about GW clustering, quantifying how effectively the AGWB traces the overdensity of CDM. The analysis of the bias of the AGWB could be complementary to the one of the anisotropies of the resolved GW sources discussed in section 3.4.1.1. The bias of the AGWB energy density can be theoretically predicted starting from the bias of the host galaxies as

$$b_{\rm GW}(z) = \frac{\int d\theta_{\rm gal} \frac{d\bar{\Omega}_{\rm GW}}{dz d\theta_{\rm gal}} b_{\rm gal}(z, \theta_{\rm gal})}{\int d\theta_{\rm gal} \frac{d\bar{\Omega}_{\rm GW}}{dz d\theta_{\rm gal}}}, \tag{3.93}$$

where $\theta_{\rm gal}$ is the key parameter describing the properties of the host galaxies. It could be the star-formation rate ψ as in [1354], or the total stellar mass $M_\star$ as in [552]. In [552] an analog expression for the bias has been given in terms of the mass function and the bias of the host halos. Since the dominant contribution to AGWB anisotropies is given by the clustering term [547, 549], even a measurement of the first few multipoles of the angular power spectrum can yield informative constraints on $b_{\rm GW}$. The astrophysical implications of the cross-correlation of the AGWB with other probes are discussed in section 4.10.6.

In addition, the cross-correlation of the AGWB with other LSS probes could play a crucial role in the detection of the anisotropies. As discussed in section 3.1.2.2, the shot noise and instrumental noise make the direct measurement of the anisotropies very challenging with current standard techniques. However, cross-correlating the GWB with other LSS tracers [546, 549, 557, 578, 589, 1352–1354], could help increasing the SNR by a significative factor. Thus, the cross-correlation with electromagnetic probes represents one of the best tools to detect GWB anisotropies with ET, if used together with the multi-frequency analysis of the anisotropies discussed in section 3.1.2.2 or other data analysis techniques. Indeed, even detecting the first few multipoles of the cross-correlation angular power spectrum would provide insights into the aforementioned underlying astrophysical and cosmological processes.

3.4.2 Cross-correlation of AGWB with CMB

Cross-correlations of GW and CMB anisotropies are an important probe for characterising the GW background and possibly disentangling its various components (e.g., the cosmological versus astrophysical contributions). The two backgrounds are indeed affected by the same large-scale (scalar and tensor) perturbations, both at production and during propagation through the Universe towards the Earth [541, 553–555, 566, 568–575, 577–579]. An overview of GW background anisotropies and their properties in the context of different early Universe scenarios can be found in section 3.1.2.1.

As discussed before, a possible source of anisotropies for the GW signal comes from the distribution of GW sources in the sky. Astrophysical GWs events, in fact, are expected to be hosted in galaxies, whose distribution follows the underlying dark matter one. Hence such sources reside in the large-scale gravitational potentials. Among the different anisotropies imprinted on the CMB signal, instead, the relevant one for the cross-correlation with GW sources is the late-times integrated Sachs-Wolfe effect [1355]. This effect arises from the

JCAP03(2026)081

evolution of gravitational potential in times: the energy of a photon going trough the potential is changed leaving an imprint on the CMB signal. The cumulative change of energy during the photon path in the dark-energy era gives rise to the late-Integrated Sachs-Wolfe (ISW) effect. This is not only a late-time effect but happens to be also relevant on the largest scales. The physical explanation for the cross-correlation, hence, becomes clear: the large-scale gravitational potential giving rise to the late-ISW are the same potentials hosting GW sources, hence tracing their distribution in the sky. The dominant contribution to the GWxCMB cross-correlation is thus expected from the density anisotropies of the former with the ISW of the latter.

The cross-correlation between GW and the CMB could also provide a complementary way to constrain primordial non-Gaussianity. As first shown by [1356–1358], the presence of local non-Gaussianities induces an additional scale-dependent term in the bias of the tracer considered. This correction affects the density term in (3.23), being the only one proportional to the GW bias [547, 552]. The scale dependence scales as $1/k^2$, hence it dominates on the largest scales. As explained above, on those scales the cross-correlation of GWs and the CMB is expected to be important and hence to be affected by the presence of non-Gaussianities, suffering of an enhancement or a suppression which can be probed by 3G detectors [576].

3.4.3 Probing LSS with GWs alone

The study of the LSS of the Universe is performed by constructing a two-point correlation function of galaxies, which describes their clustering properties at large scales ($\gtrsim 10$ Mpc). These studies are usually performed using galaxy catalogues constructed from large EM surveys. One result of these studies is the identification of the Baryon Acoustic Oscillation (BAO) peak at $\approx 100\ h^{-1}$Mpc, which puts constraints on the density parameter Ω_{m0} of the cosmological model and on the equation of state of dark energy models. We expect that the 3D localization of coalescing compact binaries could serve as another probe providing complementary information, as these compact objects trace the underlying DM distribution in a possibly different way than the luminous matter of galaxies does, due to the astrophysical processes leading up to the formation of CBCs. This discrepancy is quantified by the clustering bias. Compact binary source localizations thus probe the *GW bias* $b_{\rm GW}$, which is inherently different from the galaxy bias $b_{\rm gal}$ probed by luminous matter distribution. One should note that $b_{\rm GW}$ is potentially dependent on redshift as well as the astrophysical environment for compact binary formation and merger. It goes without saying that GW observations are needed to probe the GW bias. Earlier in this section, we have discussed the prospects of measuring $b_{\rm GW}$ using a combination of GW and EM tracers. It is worth exploring the possibility of measurement of $b_{\rm GW}$ using GW probes alone.

The proposed paradigm comes with certain challenges. Firstly, instead of point-like objects, the new method has to deal with extended GW detection volumes, which are currently of the same size or larger than the clustering scale itself. Secondly, the current GW detection rates are too low to perform this kind of statistical analysis. Hence, this endeavor requires a new detector network with enhanced sensitivity. Einstein Telescope and the 3G detector network in general open up the unique prospect of probing the LSS of the universe using GW alone.

JCAP03(2026)081

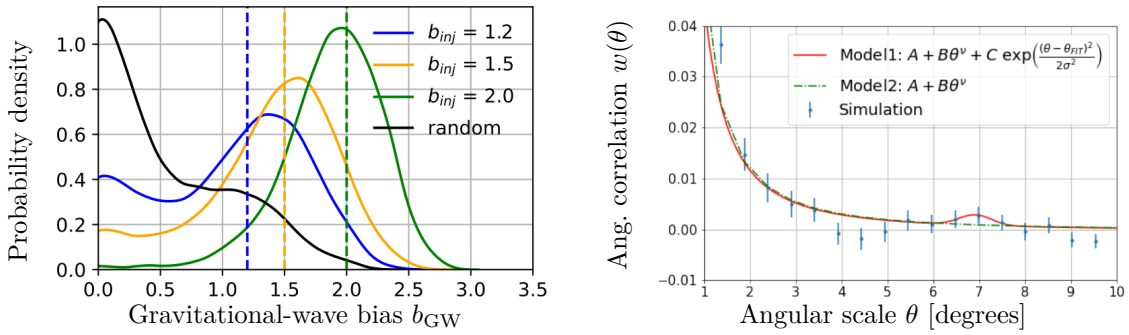

Figure 58. *Left:* recovery distributions of the GW bias b_{GW} correspond to the injected values [1359]. These results are for simulated BBH observations at a redshift $z = 0.5$ (shell thickness $350\,h^{-1}$ Mpc) and with 10 years of observation by a worldwide ET+2CE network (ET 10 km Δ + CE 40 km US + CE 40 km Australia). Reproduced from [1359]. CC BY 4.0. *Right:* recovery of the angular two-point correlation function $w(\theta)$ reveals the BAO peak at the injected angular scale, $\theta = 6.9°$ [1360]. These results are for simulated BNS observations at redshift $z = 0.3$ (shell thickness $150\,h^{-1}$ Mpc) observed by the same detector network and over similar observation times. Reproduced from [1360]. CC BY 4.0.

Using third-generation ground based detectors consisting of ET and CE, we expect to detect thousands of mergers per year with sky localization areas within a square degree. It has been shown that with 5 to 10 years of observation time with such a network, we can extract the clustering bias of the BBH population [1359] (figure 58, left panel). In that same observation time, it is possible to detect the BAO peak solely from GW observations [1360] (figure 58, right panel). This reconstruction constrains the value of H_0. Therefore, the separate galaxy and GW measurements of BAO peak are complementary to each other, and combining their data will enable us to constrain cosmological parameters using a standard ruler, i.e. the BAO scale [1361]. The results of these preliminary studies are the first indications that there are indeed prospects in probing the LSS with GW alone and more-realistic follow-up studies are in order.

Another method for probing LSS with third-generation GW observatories is by leveraging its impact on the event rate of BBHs and other CBCs [1362]. In particular, the rate of high-redshift BBHs is a sensitive tracer of the abundance of low-mass dark matter halos that form at early times. Measuring this rate therefore allows us to test for suppression in the matter power spectrum on small scales compared to ΛCDM, as predicted by various alternatives, such as warm dark matter, fuzzy dark matter, and interacting dark matter [1363]. Ref. [1362] found that a 3G network composed by ET+2CE could improve current constraints on these dark matter alternatives by as much as two orders of magnitude.

3.5 Executive summary

Here we summarize the advancements that ET will bring in Cosmology, in comparison to the current state of the art, specifically emphasizing the distinct features that the ET will allow us to explore. The following are the major areas where ET's capabilities surpass the current generation of GWs detectors.

JCAP03(2026)081

Early Universe Cosmology with Einstein Telescope

- **Gravitational Wave Background (GWB)**
  - **Sensitivity:** Einstein Telescope will provide a strain sensitivity improvement of up to a factor of 10 compared to Advanced LIGO-Virgo, achieving a targeted sensitivity of $S_h^{1/2}(f) \simeq 10^{-24}\,\mathrm{Hz}^{-1/2}$ at 10 Hz and a broader frequency range extending down to $3-5$ Hz, compared to the $\sim 10-20$ Hz lower limit of current detectors (see figure 177 for a plot of the strain sensitivity in different configurations). This expanded range will allow ET to capture more sources and trace features of the GWB that are inaccessible today.
  - **Detailed Study of GWB Components:** With its enhanced sensitivity and wider frequency range, ET will be able to:
    - **Cosmological GWB:** Detect the CGWB with a sensitivity reaching energy density values of $\Omega_{\mathrm{GW}} \sim 10^{-12}$, allowing us to probe early Universe events like inflation, phase transitions, and cosmic strings.
    - **Astrophysical GWB:** Extract astrophysical population properties more precisely, tracing large-scale structures with better sensitivity.
  - **Anisotropies and Parity violation:** with its improved sensitivity and new layout ET will have better resolution to probe anisotropies of the GWB, and will be also sensitive to chiral GWBs, which are indicators of new early Universe physics.
- **Inflation, Phase Transitions and Cosmic Strings**
  - **Inflation:** ET is expected to be sensitive to GWs originating from inflationary models beyond standard single-field slow roll and from multifield models, providing an opportunity to test fundamental physics and the presence of extra field in the early Universe.
  - **First-Order Phase Transitions (PTs):** ET is expected to be sensitive to gravitational waves originating from PTs, with an observable energy density Ω_{GW} potentially as low as 10^{-11} for strong PTs at temperatures of $\sim 10^3$ GeV, corresponding to earlier epochs of the primordial Universe with respect to those probed by LISA.
  - **Cosmic Strings:** ET will probe local string networks with tensions as low as $G\mu \sim 10^{-18}$, which is an improvement of several orders of magnitude compared to existing bounds ($G\mu \gtrsim 10^{-10}$ from current PTA experiments).

JCAP03(2026)081

Late Universe Cosmology with Einstein Telescope

- **Cosmography and Cosmological Parameters**
  - **Bright Sirens:** ET will detect hundreds of bright standard siren events (neutron star mergers with kilonovae/short GRB counterparts) per year, allowing direct measurements of the Hubble constant H_0 with sub-percent precision.
  - **Dark Sirens:** For dark sirens (BBHs without EM counterparts), ET will utilize galaxy catalog information, or correlation with the mass function, to statistically infer redshifts, enabling a $\sim 10\%$ determination of H_0 and other cosmological parameters.
  - **Distance-Redshift Relation:** The precision in measuring the distance-redshift relation will enable model-independent tests of the expansion history of the Universe, addressing current tensions in H_0 measurements.
- **Modified Gravity and New Physics**
  - **Gravitational Wave Propagation:** The ability to compare GW and EM luminosity distances will allow ET to test deviations in GW propagation that might arise from modifications to General Relativity, potentially detecting differences of order 10^{-2}.
  - **Cosmic Dipole and H_0 Tensions:** ET will also contribute to resolving cosmic dipole discrepancies by comparing dipoles in the GW and EM sectors with a precision that is unachievable with current second-generation detectors.
- **Detection of Individual Cosmological Events**
  - **Gravitational Wave Bursts from Cosmic Strings:** ET will be capable of detecting GW bursts from cosmic string cusps if $G\mu \sim 10^{-11}$, while non-detection could constrain $G\mu$ below this level for different string loop models.
  - **Primordial Black Holes:** With its improved sensitivity, ET could detect signatures from PBH mergers, originating not only from inflationary mechanisms but also from domain walls or phase transition. In this way, it will allow to shed light on Dark Matter.
  - **Ultralight dark matter:** ET will probe the existence of scalar or vector ultralight dark matter, that can form clouds around spinning black holes.

Einstein Telescope will provide a significant step forward in our ability to study our early and late Universe. It will offer deeper insight into processes occurring at high redshifts and across a broader range of frequencies than ever before, making it an essential tool in the pursuit of our understanding of cosmology.

JCAP03(2026)081

4 Population studies and astrophysical background

The first detection of gravitational waves (GWs) in 2015 is often compared to Galileo's first astronomical observation with an optical telescope. Moving from LIGO-Virgo-KAGRA to the Einstein Telescope (ET) and Cosmic Explorer marks an equally transformative leap, comparable to advancing from Galileo's crude instrument to the James Webb Space Telescope, which now reveals the cosmos in unparalleled detail. ET will observe approximately 10^5 binary black hole (BBH) and $10^4 - 10^5$ binary neutron star (BNS) mergers every year, up to a redshift of 100, and for a few thousand BBH events per year and several tens to $\mathcal{O}(10^2)$ BNS per year, the signal-to-noise ratio will exceed 100 [16, 1167]. With such capabilities, ET will unveil the mass function and spin distribution of BHs and neutron stars (NSs) in exquisite detail, allowing us to probe their evolution with redshift. While LIGO and Virgo have already paved the way for studying intermediate-mass BHs ($10^2 - 10^5 M_\odot$) with GWs, ET will observe systems with masses of $\approx 10^3 M_\odot$ up to a redshift of ≈ 8, possibly via joint multi-band observations with LISA, the first space-borne GW detector. This will be pivotal for understanding the formation of supermassive black holes in the Universe.

At high redshift, Population III stars, the very first stars formed in the Universe, continue to elude our observations, even with the James Webb Space Telescope. The Einstein Telescope will routinely observe mergers of black holes born from Population III stars, with the main challenge being distinguishing such high-redshift messengers from other events. The individual observation of a binary BH merger at redshift $\gtrsim 30$, or of a sub-solar mass non-tidally deformable object would be a smoking gun for the existence of primordial black holes, with profound implications for our understanding of dark matter. This will ultimately pave the way for interpreting the formation channels of binary compact object mergers.

4.1 Introduction: formation channels of binary compact objects

After three observation runs, the LVK detected ~ 100 compact binary coalescences (CBCs, [6]), a number that may double or triple by the end of the ongoing fourth observation run. The number of detected CBCs enabled the scientific community to start placing constraints on the properties of the underlying population of compact objects. Nonetheless, the origin of CBCs is still unknown and widely debated. Broadly speaking, we can distinguish two main formation channels: the isolated channel, according to which compact binaries are the byproduct of binary stellar evolution; and the dynamical channel, in which compact binaries — or their progenitors — pair up through gravitational interactions in dense stellar environments. ET will contribute key improvements to reveal the formation channels and distinguish between them, for example through golden (high SNR) events that will pin down properties currently difficult to measure like spin, as well as through multidimensional constraints, such as the redshift dependence of masses and spins. Here below, we discuss this in detail.

4.1.1 Isolated channel: compact binary mergers from pairs and multiples in galactic fields

4.1.1.1 Binary evolution with mass transfer. For most close binaries, it can become unavoidable for the two stars to interact at some point during their life to eventually form a GW source. A circular binary with two compact objects can only experience a merger due to

JCAP03(2026)081

GW emission within a Hubble time if the orbital separation is less than a few solar radii (for NS+NS) to less than several tens of solar radii (for BH+BH) [1364]. However, the radius of their progenitor stars is already larger than a few solar radii at birth, and easily reaches tens to hundreds of solar radii during the giant phases [1365]. For that reason, the story of the formation of GW sources in stellar binaries is one of stellar interactions and mass transfer.

A mass transfer phase strongly affects the stellar components (i.e., their masses and mass ratio, their spin properties), as well as the orbital separation, and consequently the delay time (i.e. the time elapsed from binary formation down to the merger). Progenitors of CBCs typically undergo two mass transfer interactions: a first one in which the initially most massive (primary) star is stripped of its hydrogen envelope, and the second one where the companion star is stripped. If the process occurs in a self-regulating manner, it is referred to as "stable mass transfer", while "unstable mass transfer" is often assumed to lead to a common-envelope (CE) phase [1366–1369]. Interestingly, the process of stable and unstable mass transfer affects the system in different ways, leaving different imprints on the system. These imprints provide us with a wonderful opportunity to distinguish between (or potentially determine the) GW progenitors from the source properties. Here we mention the two main channels in binary evolution with mass transfer and discuss the corresponding source properties. Other channels likely make up only a few per cent of the total yield (e.g., [1370, 1371]).

Common envelope channel. A well-known evolutionary pathway is the common-envelope channel (hereafter CE channel: an example is given in figure 59, left). This channel leads to plenty of BBH mergers [1372, 1373], BHNS mergers [1370, 1374, 1375], as well as BNS mergers [1374, 1376–1378]. Initially on the zero-age main-sequence (ZAMS), the stars are not interacting (stage 1). After expanding, the primary star fills its Roche lobe and the first phase of mass transfer commences (stage 2). It proceeds in a stable manner, typically leading to widening of the orbit. The donor star is slowly stripped of its envelope, and at the end of its nuclear evolution, it will collapse to a compact object (i.e. BH or NS) at stage 3 (see also section 4.3.3.1). The next stage in the channel is driven by the evolution of the secondary star, leading to a second phase of mass transfer at stage 4 (see also section 4.4.1). For this channel, the second phase of mass transfer occurs in an unstable manner due to the extreme mass ratio and the response of the donor to mass loss, and a common-envelope phase is expected to develop. The name of the channel is derived from this second phase of mass transfer. During the common-envelope phase, the companion plunges into the envelope of the secondary star, and continues spiraling in due to friction. A merger is avoided if and when the envelope becomes unbound and is ejected from the system. The remaining binary has a much reduced orbital separation. In case of BHNS and NSNS formation, the secondary star may fill its Roche lobe a second time as a hydrogen-poor helium-star (i.e. case BB Roche Lobe Overflow), before collapsing to a NS. At stage 5, the system consists of two compact objects in a close orbit. Due to GW emission, the orbit shrinks further, eventually leading to a double compact object merger (stage 6).

Stable mass transfer channel. The stable mass transfer channel differs from the CE channel in only one key aspect [1375, 1379–1381]; the second phase of mass transfer (stage 4) does

JCAP03(2026)081

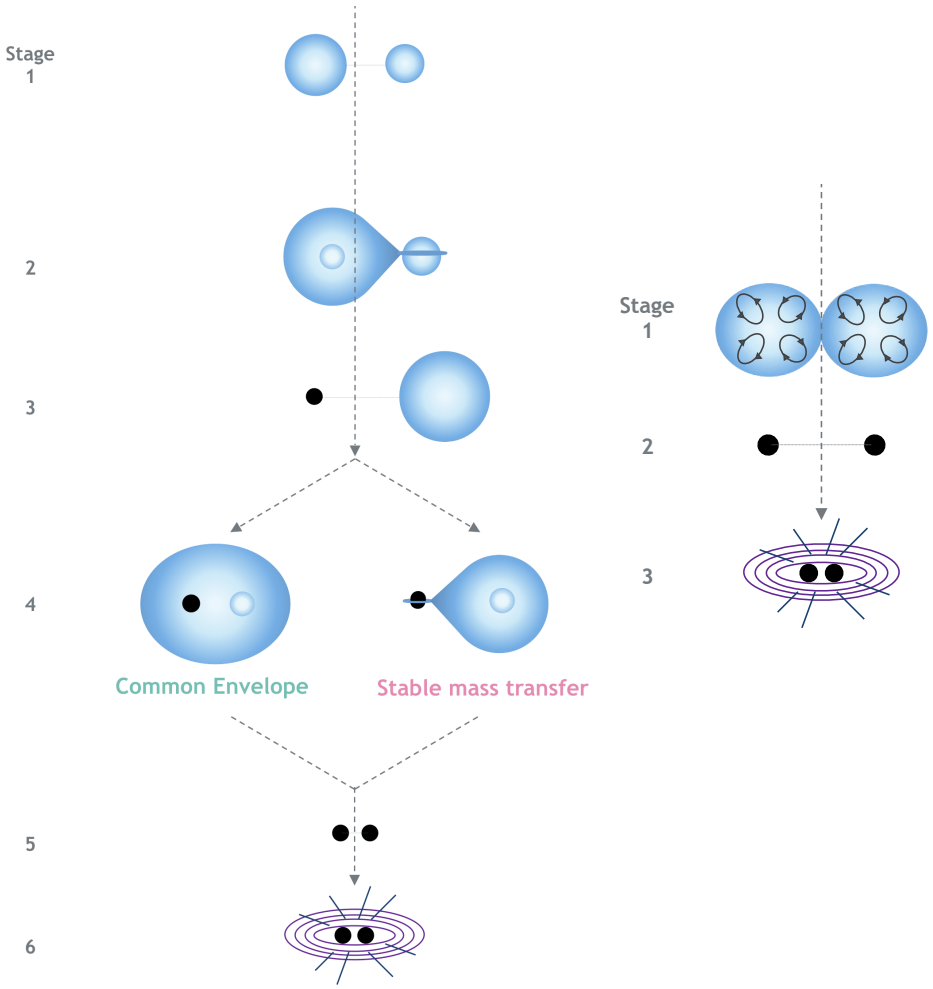

Figure 59. Evolutionary pathways to form a GW source for isolated binary evolution. *Left:* the common-envelope channel and the stable mass transfer channel. Stage 1) Zero-Age-Main-Sequence (ZAMS) 2) First phase of mass transfer 3) Formation of BH or NS 4) Second phase of mass transfer 5) Formation of double compact object 6) GW merger. *Right:* chemically homogeneous evolution. Stage 1) ZAMS 2) Formation of binary BH 3) GW merger.

not lead to a CE-phase, but in fact the mass transfer is self-regulating and therefore proceeds in a stable manner (stage 4 in figure 59).

It is important to realise that in order to form a GW merger, this second phase of mass transfer should lead to a shrinkage of the orbit. This occurs for those systems that have relatively high mass ratios (i.e. the secondary star is more massive than the compact object) and that experience relatively large angular momentum loss compared to their mass loss, as expected for a BH accretor. As the compact object binaries tend to be wider at formation (stage 4 in figure 59) than for the classical CE-channel, the stable channel typically leads to GW events with longer time delays [1382, 1383].

GW signatures. As the GW sources from isolated binary evolution can be formed through multiple sub-channels (e.g., CE channel and stable mass transfer channel), one can ask: what is the relative contribution of each channel? Historically, binary evolution calculations

JCAP03(2026)081

have found that the CE channel dominates the total merger rate [1371, 1384]. However, recently there are indications that its contribution to the BBH merger rate may have been overestimated [1385–1389]. These works suggest that the common envelope may not be successfully ejected (stage 4 in figure 59) in many binaries, but instead leads to a merger or to stable mass transfer. The level of mixture between the channels therefore depends on the assumptions made when modeling binary evolution [1371, 1390, 1391].

ET can play an important role in distinguishing formation channels, since the intrinsic level of mixture is very likely redshift-dependent. As the stable channel typically leads to binary compact objects with relatively wide orbits (see above), its GW sources have longer delay times ($t_{\rm delay} \gtrsim 1$Gyr) merging predominantly in the local Universe. Correspondingly, binary compact objects from the CE channel are born with more compact orbits, and merge with shorter delay times ($t_{\rm delay} \lesssim 1$Gyr) and higher redshifts on average. It is found that the BBH merger rate from isolated binary evolution is dominated by sources from the CE channel at large redshifts, while in the local Universe the contributions from the CE and stable channel are similar [1383, 1392].

In addition ET can put constraints on the physics of the CE phase that is poorly understood [1368] by inferring from the merger rate the size of the post-CE orbits that depends on the efficiency of the deposition of energy into the envelope, in particular for BNS[30] mergers [1393]. This is not possible with current instruments, given the limited redshift coverage, even with the help of precise redshift determinations from electromagnetic counterparts.

There are also correlations between the formation channel and the compact object masses that ET can uncover. For example, the typical mass ratio of BBHs formed through the stable mass transfer channel range between 0.6–0.8, whereas the CE channel provides sources with a relative flat mass ratio distribution between[31] 0.2–1.0 [1374, 1375, 1382, 1383, 1394]. Similarly, the mass ratio of BHNS ($M_{\rm NS}/M_{\rm BH}$) peaks at ~ 0.3 for the stable channel, and spans from 0.1 to 0.5 for the CE channel [1370, 1374]. In addition, there is a link between the BH mass, the delay time and the formation channel of BBH mergers [1383, 1390, 1395, 1396]. The CE channel preferentially produces BHs with masses below about $30M_\odot$, while the stable channel primarily forms systems with BH masses above $30M_\odot$. As BBH mergers from the stable mass transfer channel typically merge with long delay times, mergers of massive BHs are expected to predominantly occur at low redshifts and be relatively less common at higher redshifts. This counter-intuitive result holds despite the fact that massive BHs are easier to form at low metallicities which are more common at higher redshifts [1383, 1395, 1397].

4.1.1.2 Chemically homogeneous evolution (CHE). An example of non-mass-transfer binary evolution is chemically homogeneous evolution [1398–1400]. In the context of GW progenitors, the CHE scenario considers compact binaries that are near contact or even in contact at the start of the hydrogen burning phase (see stage 1 in figure 59, right panel [1401–1405]). In such binaries, tidal interaction will enforce rapid stellar rotation, which in turn induces meridional currents in the radiative layers of the rotating star [1406–1408]. The

[30] It is advantageous to use BNS over BBH or NSBH, as the BNS merger yield is virtually independent of metallicity [1374, 1375, 1377].

[31] The shape of the mass distribution depends on the CE efficiency [1374, 1382].

JCAP03(2026)081

mixing currents prevent the build-up of a chemical gradient inside the star and keep the star chemically homogeneous during most of the core hydrogen burning phase. Contrary to classically evolving (i.e. slowly rotating) stars, chemically homogeneously evolving stars do not experience significant expansion during the post-main-sequence phase. After the core hydrogen burning phase ends, the stars will become helium-burning stars, before collapsing to a black hole (stage 2). The binary black hole then merges due to GW emission (stage 3).

GW signatures. For the CHE scenario to produce mergers in a Hubble time, stellar winds need to be weak, as is expected at low metallicity [1409, 1410]. The reason for this is threefold: 1) stellar winds cause a spin-down of the star which halts rotational mixing, 2) stellar winds cause a widening of the orbit in which a tidally locked star has to spin down, 3) the widened orbit may be too wide to merge within a Hubble time due to GW emission alone. Therefore we expect the CHE channel to take place only at low metallicities. In addition, as the wide orbits give rise to long delay times, mergers at high redshifts are less likely to be observed for this channel in comparison with the classical channels (e.g. [1392]). Lastly, naively one may expect large effective spins from this channel due to the high rotational velocities required for the stars. However, Marchant et al. [1403] argue for moderate spins ($\sim$0.4) due to stellar winds during the Wolf-Rayet phase.

Other signatures that may be used to distinguish events from the CHE channel from other channels are related to the expected masses. In the CHE channel, there is a strong preference for high mass black holes ($\gtrsim 25M_\odot$) as CHE is not effective for lower mass progenitors [1411]. Therefore, it only produces binary black hole mergers, and not binary neutron star or BH-NS mergers. Secondly, there is a preference for detecting events with nearly equal-mass components [1402, 1403]. ET will thus be able to determine if a population of BBH with these properties exists or not.

The CHE channel is competitive with the classical isolated binary evolutionary channel with respect to rates [1402–1405] (see also section 4.2 for a discussion on rates and their large uncertainties). In particular, Riley et al. [1405] showed that the CHE channel may contribute 50–75% of all aLIGO BBH detections from isolated binary evolution. For the highest chirp masses ($M_{\rm chirp} > 30M_\odot$), this percentage may be as high as 80%.

ET can also measure the effective inspiral spin parameter, $\chi_{\rm eff} = (m_1\vec{s_1} + m_2\vec{s_2})/(m_1 + m_2) \cdot \hat{\mathbf{L}}$, where $\vec{s_1}$ and $\vec{s_2}$ are the dimensionless spins of the two components, while $\hat{\mathbf{L}}$ is the orbital angular momentum versor. For isolated binary evolution, at first sight it does not strongly constrain the formation channels in isolated binary evolution. This is because the effective spin is predominantly determined by the natal BH spin and the orientation of the BH spins [1412, 1413]. If angular momentum is transported efficiently through the progenitor star, the resulting BH natal spin is low, as preferred by current-day GW observations (e.g., [1414, 1415]). Low effective spin is also possible if the BH spins are misaligned. It is possible to form GW sources with high spins in isolated binaries if the stellar angular momentum transport is inefficient, or by increasing BH spins through accretion [1382, 1416–1418] or through tidal interactions [1392, 1419–1421]. Interestingly, the latter implies a relation between the effective spin and the redshift of the merger that should become visible with third-generation instruments [1392]. The fraction of highly spinning BBHs from isolated binary evolution is expected to increase with redshift, as low metallicity stars experience less

JCAP03(2026)081

wind mass loss and less radial expansion, enabling the formation of more compact binaries with stronger tidal interaction and prompt GW mergers. At low redshift ($z \sim 0.5$ i.e., in the currently observable population) highly spinning BHs are expected to be dominated by BHs formed through chemically homogeneous evolution. In addition, for low CE efficiencies that translate to tighter post-CE orbits and more strongly spun up BHs, the highly spinning BHs in the CE channel merge at high redshifts ($z \sim 2$) close to the peak of the cosmic star formation rate, but outside current detector horizons [1382]. The advent of third-generation instruments would finally enable us to detect the redshift dependence of the intrinsically highly spinning BBH population from isolated binaries. This would enable us to clearly identify the population of BBHs that are of isolated origin.

4.1.1.3 Evolution in higher order systems. Observations of massive stars in the Milky Way and the Magellanic Clouds suggest that their companion fraction is high; typically massive stars not only have a stellar companion, but two or three companions [1422–1427]. It is therefore interesting to ask if and how this may change the GW signatures compared to isolated binary evolution. In the following section, we consider the evolution of small and isolated stellar systems.

Non-interacting triples. If both the inner and outer orbit are sufficiently wide that mass transfer will not take place, the stars evolve as if they were single stars. After a triple compact object has been formed, the system experiences strong three-body dynamical effects such as von Zeipel-Lidov-Kozai cycles [1428–1430]. During these cycles, the eccentricity of the inner binary can reach high values, which enhances the GW emission and can lead to a merger [1431–1439]. The predicted BBH merger rate for this channel events is estimated at $\sim 0.5 - 5$ yr^{-1} Gpc^{-3} for solar metallicity and 25/yr/Gpc^3 at low metallicity. Due to the strong impact of supernova kicks, the rate for NSBH mergers is more uncertain, $10^{-4} - 25$ yr^{-1} Gpc^{-3} [1438, 1439].

Interacting triples. When the orbits are closer, triples do experience mass transfer at some point in their evolution (right column in figure 60, see [1440–1443]). The existence of a tertiary star can lead to an earlier interaction in the inner binary, a merger of the inner binary turning the triple into a binary system, or even multiple mergers in case of higher-order systems. In a third of the triple systems, the tertiary plays a fundamental role in the evolutionary pathway, leading to configurations that are not predicted for isolated binaries. The predicted merger rate in this channel can reach 25 yr^{-1}Gpc^{-3} (e.g. [1444]).

GW signatures. The GW signatures of these mergers are high eccentricity [1433, 1445] and a mass ratio q-distribution that is significantly flatter than for isolated binary evolution or for dense stellar clusters [1436, 1444, 1446, 1447]. Multiple mergers can produce masses in the upper and lower mass-gap [1448–1452], see also section 4.3. Moreover, in triples with chemically homogeneously evolving inner binary stars, commonly the third star will transfer mass to the inner binary black hole [1447], possibly leading to "wet" mergers in which the orbital decay is driven by gas drag instead of GW emission [1453]. Of particular interest is the effect of triple stars on the effective spin of BBH mergers. Although complicated by GR effects, many studies have found that, independently of their magnitude, the coupling of

JCAP03(2026)081

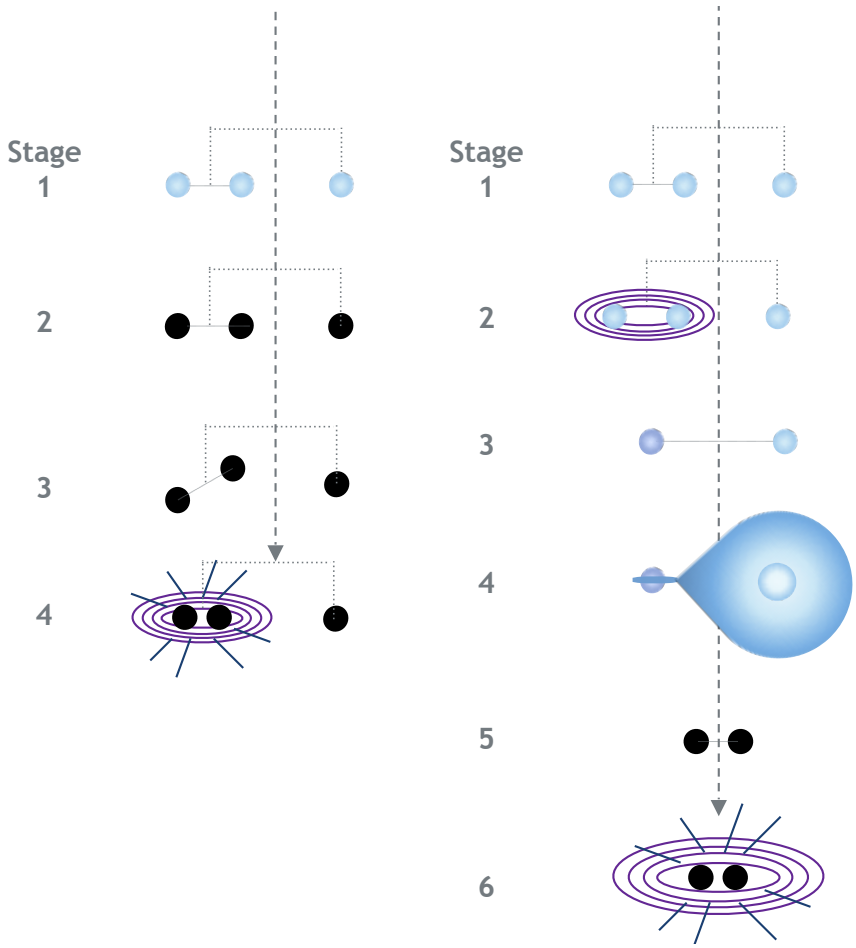

Figure 60. Evolutionary pathway to form GW sources a) according to the non-interacting triple channel, b) in an interacting triple with a stellar merger in the inner binary. On the left: Stage 1) ZAMS 2) Formation of triple BH 3) ZLK cycles and orbital dissipation 4) GW merger. On the right: Stage 1) ZAMS 2) Stellar merger in the inner binary 3) Formation of binary with a rejuvenated star 4) Various phases of mass transfer 5) Formation of binary BH 6) GW merger.

triple dynamics with GW energy loss leads to misaligned spins and $\chi_{\rm eff} \sim 0$ [1435, 1437, 1439, 1445, 1454–1457]. ET will be able to uncover a significant population of mergers originating in triple systems (e.g., [1458]).

4.1.2 Dynamical channel: stellar systems as factories of merging compact objects

With densities much larger than galactic fields, star clusters represent ideal factories for the production of dynamical CBCs. Theoretical models and observations generally gather clusters into three main categories: open and young massive clusters, with typical masses in the range $10^2 - 10^5 M_\odot$ [1459], globular clusters ($\sim 10^5 - 10^7 M_\odot$) [1460], and nuclear clusters ($10^6 - 10^8 M_\odot$) [1461]. A primary difference among different cluster types is the typical density, which varies from $< 10^4 M_\odot$ pc^{-3} in open clusters [1459, 1462] and can reach extreme densities of $10^8 M_\odot$ pc^{-3} in the densest nuclear clusters [1463]. Additional differences pertain

JCAP03(2026)081

to the possible presence of gas in young clusters, the development of multiple populations in globular clusters, and the peculiar star formation history or the possible presence of a central supermassive black hole in nuclear clusters.

Within the dynamical scenario, there is a large variety of processes that can lead to the formation of CBCs, as we briefly describe in the following. The branching ratio of such processes intrinsically depends on the binary properties and the cluster type and structure.

Dynamical formation in a star cluster is expected to be more effective for BBHs than for both BNSs and NSBHs, because BHs dominate the dynamics in the cluster central regions, preventing the segregation of NSs and their progenitors and suppressing their interaction rate.

As the star cluster evolution proceeds, though, BHs are slowly evacuated from the cluster in what is called the BH burning process [1464]. As the number of BHs diminishes, the probability for NSs to interact with other BHs and among each other increases. Therefore, theoretical models predict that the number of NSBH and BNS mergers with a dynamical origin is much smaller than that of BBHs, and their occurrence requires that the host cluster lost a significant fraction of its original BH population [1465–1469].

Despite their rarity, a subpopulation of dynamical NSBH mergers may exhibit characteristic features that differentiate them from the isolated ones. These include BHs heavier than $10M_\odot$ [1467, 1470], a chirp mass $> 4M_\odot$ [1468], the absence of an electromagnetic counterpart [1468, 1471, 1472], and longer delay times, with most of them likely forming over a cluster relaxation time [1466, 1470].

BNS mergers are even rarer than NSBH and their occurrence in star clusters is expected to be several orders of magnitudes smaller than in the field [1466, 1473]. Given their rarity, it is also unclear whether dynamical BNS mergers can exhibit distinctive features compared to those forming in galactic fields [1467, 1474]. Most likely, the only way to infer a dynamical origin is via the association of the resulting EM counterpart with a dense cluster.

Moreover, the low detection rate of both BNS and NSBH by current ground-based detectors, alongside with the limited number of BNS detected through other means of observation, make it hard to assess the existence of a "lower mass-gap" separating NSs and BHs, in the mass range $2-5M_\odot$. In this sense, the recent discovery of a CBC by the LVK Collaboration involving a NS and an object with a mass in the range $2.5-4.5M_\odot$ [1475] could make the case for a dynamical origin [1467, 1474, 1476] or push new studies to explore more some poorly understood mechanism of stellar evolution, like the common envelope physics [1477].

4.1.2.1 How can CBCs form in star clusters and merge within a Hubble time.

Primordial binaries. The simplest way to form CBCs in a star cluster is from the evolution of binary stars already paired at birth, the so-called "primordial binaries". Observations of stellar nurseries and young star clusters suggest that up to $50-70\%$ (and even 100% in some extreme cases) of stars are born in binary systems and higher-order multiples [1423, 1424]. The binary fraction seems to increase with the primary mass [1423], thus suggesting that many, if not all, compact object progenitors may have been part of a "primordial" binary.

At the simplest level, the binary star can evolve into a CBC via stellar evolution making it indistinguishable from the same binary evolving in isolation. If, however, the timescale

JCAP03(2026)081

for binary–single stellar interactions is shorter than the binary delay time, the perturbations induced by stellar flybys and close encounters on the orbit can significantly alter the binary evolution, either shortening its merging time or delaying it, leading to a swap between an interloper and one of the binary components, or causing its ionization.

Even in the extreme case that no stars are born in a binary system, there are several ways to form CBCs via dynamics.

Gravitational wave captures. If the two CBC components, initially unbound, undergo a close hyperbolic encounter, GWs emitted during the passage at pericentre (GW bremsstrahlung) can carry away enough energy to bind the two objects. This process, called gravitational wave capture, requires an environment with densities typical of galactic nuclei [1478, 1479] and dense globular clusters [1480, 1481]. In this scenario, the pericentre distance between the two objects must be so small that CBCs forming through this channel merge minutes to hours after the interaction [1478]. Given their short formation time, their merger rate will directly follow the binary formation rate, which is expected to be in the range $0.2 - 150$ Gpc^{-3} yr^{-1} [1482]. Up to 90% of mergers formed this way can retain an eccentricity $e > 0.9$ at 10 Hz [1478, 1483–1485].

Three-body binary formation. Another way to form tight binaries is via three-body binary formation. In this case, three initially unbound objects find each other and closely interact up to the point that two objects pair up and the third carries away the extra energy. The timescale of this process is extremely sensitive to the cluster velocity dispersion, being $\propto \sigma^9$ [1486], and generally exceeds a Hubble time for the densest globular clusters and nuclear clusters. Nonetheless, three-body binary formation represents a primary channel to build-up hard binaries, i.e. binaries with a binding energy larger than the average kinetic energy of the environment [1487], containing at least one compact remnant [1488, 1489], but see also [1490]. Such binaries can either merge outside the cluster or harden via binary–single and binary–binary interactions.

Binary–single interactions. If the cluster harbours a population of binaries, either primordial or formed via three-body interactions (see paragraph above), CBCs can form through interactions between the binary and a third compact object (binary–single interactions) depending on the binary dynamical status (i.e. if it is hard or soft) and the star cluster structure and evolution [1491, 1492]. This type of interaction can account for up to $20 - 70\%$ of all mergers occurring in Galactic nuclei [1493], and is a primary mechanism for forming CBCs with large eccentricity (e.g., [1492, 1494–1496]) or with at least one component in the lower or upper mass gap by triggering the merger of the inner binary system [1497–1499].

When the distance between a binary and an incoming third body falls below a few times the binary semimajor axis, the three bodies can undergo a so-called *resonant* interaction, a chaotic phase during which the three bodies pair up and exchange continuously (e.g., [1500–1502]). This process proceeds up to the point in which one of the objects, generally the least massive, is expelled and the other two form a hard binary [1465, 1468, 1490, 1496, 1502].

Gas-driven dynamics. Star clusters rich in gas, such as embedded open clusters or young massive clusters, can nurture the development of CBCs as the gaseous medium can alter

JCAP03(2026)081

the orbit of a binary, for example by inducing a dynamical friction term on the components that shrinks the binary and can enhance the probability for the binary to merge within a Hubble time [1503].

Gas-driven CBC formation can also occur in the dense disks that surround AGNs [1504–1506]. In such extreme environments, the disk can dissipate the orbital energy of compact objects passing through its medium and capture them, thus their orbits settle in the plane of the disk and undergo inward migration that steepens the radial density profile around the SMBH [1507]. The aforementioned process acts faster than relaxation in AGN disks, and can nurture the formation of CBCs in the plane of the disk aided by a combination of gaseous accretion, gas dynamical friction, and stellar scattering [1482, 1505].

In the case of BBHs, it has been suggested that mergers occurring in an AGN can power an EM counterpart [1508]. GW190521, the first GW source to produce a final mass in the intermediate-mass black hole (IMBH) range ($\sim 150 M_{\odot}$) [1509], has been associated with a high-energy transient detected by the Zwicky Transient Facility [1273], although it is rather hard to assess whether this association can be robustly confirmed [1274].

Secular mechanisms. Secular effects generally develop when the binary is perturbed by a third object or a series of close passages by different objects. Depending on the perturber orbital properties, the binary can undergo Kozai-Lidov oscillations [1429, 1430], a mechanism that could boost the merger probability of CBCs in dense clusters [1510–1512] and galactic nuclei [1513–1518]. Weak perturbations acting on soft binaries in loose star clusters, for example, can induce a steady increase of the binary eccentricity on a timescale shorter than the binary evaporation time, up to the point that the binary coalescence occurs within a Hubble time [1519, 1520].

4.1.2.2 Properties of dynamical CBC. Dynamical CBCs exhibit peculiar properties, some of which may be unique marks of this formation channel, as we briefly discuss in the following.

Eccentricity of dynamical CBCs. Several works have pointed out that orbital eccentricity may represent a key parameter to identify dynamical CBCs, as according to most stellar evolution theories, isolated CBCs are expected to circularise before reaching the Hz frequency band [1521]. Moreover, eccentricity could be used to untangle the population of mergers occurring after their ejection or inside a cluster, either triggered by repeated interactions or owing to hierarchical secular dynamics [1495, 1511, 1522–1524]. In general, we expect that in-cluster mergers are more eccentric than mergers occurring after the ejection of the CBC from the parent cluster [1522, 1523].

The different eccentricity distribution for in-cluster and ejected mergers may be particularly evident in the 1–10 Hz frequency band. In-cluster mergers forming from three-body and binary–single interactions have typical eccentricity in the $10^{-4} - 10^{-2}$, whilst those forming from GW captures have very high eccentricities, > 0.9, and merge on timescales of days or years. In the case of ejected binaries, instead, their eccentricity may be too small $< 10^{-5}$ to be accurately measured in the $1 - 10$ Hz band, and a detector sensitive at lower frequencies could be more suited to detect them. In these regards, the possibility to access the $0.001 - 0.1$ Hz fre-

JCAP03(2026)081

quency band, for example with LISA, DECIGO, or the LGWA, could enable us to observe the eccentricity evolution of the binary weeks to months prior to the merger, helping us to place constrain on the origin of stellar mass CBCs. However, particular attention is needed when modeling the signal, owing to the spin precession-eccentricity degeneracy [1525, and reference therein], which can significantly hinder eccentricity measurements (e.g., [1525–1527]).

Stellar interactions, hierarchical mergers, and spins. A binary traveling in a stellar environment is subjected to binary–single interactions that can impart on its motion a Newtonian recoil and remove part of the binary orbital energy. As a consequence, the binary progressively shrinks (*hardening* process), making the new interactions rarer but more violent [1487]. At some point, GW emission takes over and drives the binary to coalescence inside the cluster, provided that the binary shrinking rate due to GWs is larger than the binary–single interaction rate. Otherwise, a new interaction can, on the one hand, increase the binary eccentricity and possibly trigger a rapid GW coalescence, and, on the other hand, transfer enough kinetic energy to expel the binary, which then will merge outside the cluster.

Using the population synthesis code B-Pop [1528], we show in figure 61 how the fraction of in-cluster mergers varies with the cluster escape velocity, calculated at the time of the binary merger for different assumptions about the initial binary semimajor axis distribution. Specifically, we either assume a Gaussian distribution peaked around the hard-binary separation [1502] with dispersion $\sigma_a = 0.1,\ 0.3$, or a flat distribution between 0.1–0.2 AU [1480]. B-Pop models are compared against direct N-body [1524, 1529] and Monte Carlo simulations [1495]. Note that for all the simulation database considered, the fraction of in-situ merger is calculated taking into account only dynamically assembled binaries, and the range of simulated velocity dispersion is shown, generally limited to within a factor of a few from the average value. Despite B-Pop relies on an approximated method to simulate BBH mergers, their results agree surprisingly well with both few-body and self-consistent simulation of star clusters. In general, it is evident that the fraction of in-cluster mergers sensibly increases with the cluster escape velocity, especially in the case of tight BBHs [1481, 1530–1533]. This aspect can have crucial implications for the development of multiple mergers and the formation of higher-generation BHs, as we discuss in the next section.

Asymmetries in the emitted GW signal impart a relativistic kick on the merger remnant [1534–1536]. If the amplitude of such recoil is smaller than the cluster escape velocity, the remnant can remain in the cluster and merge again, leaving behind a second-generation remnant. The development of repeated mergers is usually referred to as the hierarchical merger mechanism [1491]. Relativistic kicks can be as large as $10^4\,\mathrm{km\ s^{-1}}$, therefore hierarchical mergers are expected to develop only in the most massive and dense star clusters [1481, 1491, 1528, 1537–1546], especially because the escape velocity of star clusters decreases over time owing to relaxation processes, which cause mass-loss and expansion [1528, 1542, 1547].

Higher-generation BHs are expected to be characterised by clearly different spins compared to first-generation mergers. For example, second-generation mergers are expected to have dimensionless spin distribution tightly peaked around $\chi \sim 0.7$ [1548–1550]. The ability to identify a second-generation merger thus depends on the natal spin distribution of their progenitors [1528, 1551, 1552]. For higher generation remnants, instead, the older the

JCAP03(2026)081

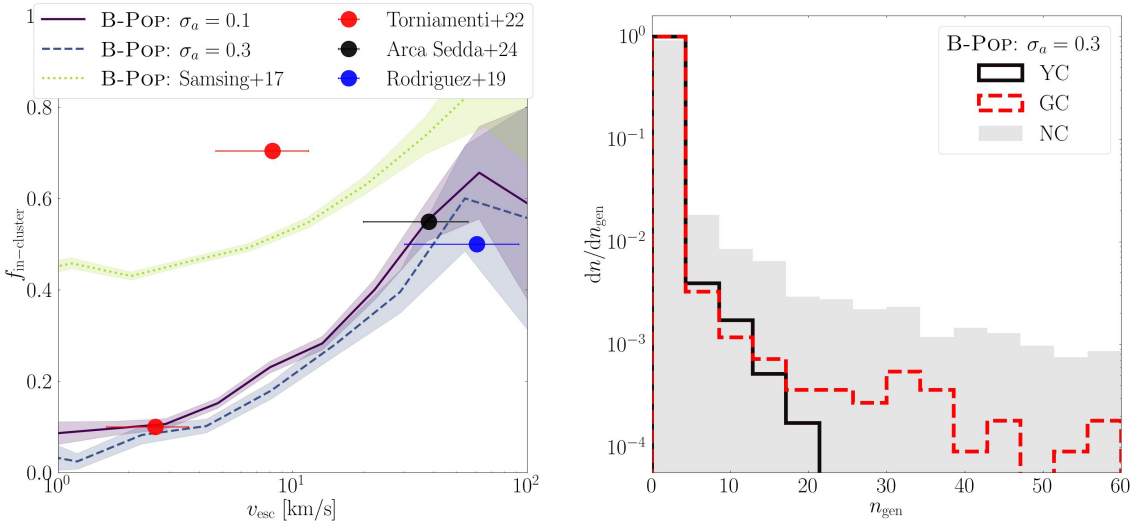

Figure 61. *Left panel:* fraction of BBHs that merge inside the cluster for different assumptions about the binary semimajor axis sampling: assuming a Gaussian distribution peaked around the hard binary separation with $\sigma_a = 0.1$ (purple straight line), or with $\sigma_a = 0.3$ (blue dashed line), or following the assumption of [1480], i.e. that a is distributed between $0.1 - 0.2$ AU according to a flat distribution. Shaded areas encompass the Poissonian error associated with the samples. The points represent data from self-consistent N-body and Monte Carlo simulations of star clusters. *Right panel:* distribution of merger generation for different cluster types. All models are performed with the B-Pop population synthesis tool [1528].

generation the smaller the spin [1538, 1553]. Higher generation merger remnants also feature typical precessing spin values $\chi_p = 0.5 - 0.8$, which are hardly achievable with isolated and 1st generation mergers [338, 1542, 1554, 1555].

The mass, spin, and generation of a hierarchical merger product encode information about the host cluster and the properties of the previous chain of mergers. For example, the GW recoil is generally smaller if the merging components have small spins, therefore the development of a long merger chain requires a natal spin distribution that favors low spins [1481, 1532]. The amplitude of the kick requires a host environment with a large escape velocity, generally $> 100\,{\rm km\ s^{-1}}$, thus favoring dense and massive globular and nuclear clusters as preferred environments for higher generation merger products [1528, 1530, 1543, 1553, 1556].

The hierarchical merger mechanism represents a viable way to form IMBHs (see section 4.8 and references therein) and BHs in the upper mass gap [1488, 1491, 1499, 1524, 1539, 1540, 1544, 1557–1560]. Upper mass-gap BHs can also form via stellar evolution under particular conditions [1561–1564] or via stellar collisions [1395, 1499, 1524, 1565–1567]. Mergers involving upper mass-gap BHs can thus carry information about their formation origin. Precise measurements of masses and spins could help untangle different formation channels for mergers involving one or two BHs with masses in the gap. In this sense, at masses below $O(500M_\odot)$ ET will enable to place stringent constraints on the primary spin, chirp mass, location and distance [16, 107, 1167, 1181, 1568, 1569], offering a unique opportunity to infer the origin of mergers with one or both components in the upper mass gap.

JCAP03(2026)081

4.1.3 Fingerprints of different formation channels

As we have seen in the previous sections, CBCs forming from the isolated and dynamical channels exhibit some peculiar features that could be used to infer the contribution of different channels to the cosmic population of CBCs [338, 1528, 1570]. With the prospective detection of 10^5 BBH and BNS events per year [16, 1167], it will be possible to characterise in detail the impact of the isolated and dynamical channels on the formation of CBCs. This can be achieved by constraining crucial quantities like merger rates, redshift dependencies, masses and spins of merging CBCs.

Merger rates are highly uncertain, as they depend on the cosmic star formation history, the metallicity evolution, and the star cluster formation process. Isolated binary models predict a BBH merger-rate density $\mathcal{R} \sim (0.5 - 5,000)\,\mathrm{yr}^{-1}\mathrm{Gpc}^{-3}$ at redshift $z \lesssim 1$, while dynamical models suggest $\mathcal{R} \sim (10^{-3} - 10^{2})\,\mathrm{yr}^{-1}\mathrm{Gpc}^{-3}$ (for a comprehensive discussion about rates from different channels, [1482, 1571]). A similar difference in the expected merger rates is also estimated for BHNS mergers, while for BNS most models suggest that isolated mergers outnumber dynamical mergers by one order of magnitude, despite the large uncertainties [1571]. Note that the upper limits to theoretical predictions are already in tension with the local merger-rate densities inferred from LVK data [7]. See also section 4.2 for further details about CBC merger rates. With ET, we will be able to verify the possible evolution with redshift of the merger rate [7] and other quantities, like the median mass or the primary mass of merging BBHs [1528, 1542, 1572], and their mass ratio [7].

The binary mass, primary mass, and mass ratio distributions can be diagnostic quantities to unveil features from different channels. For example, mergers with large primary mass and low-mass ratios are most likely byproducts of dynamical processes [1466–1468, 1481, 1491, 1528, 1537–1546], while isolated mergers predominantly favor the formation of lower mass mergers [1370, 1395, 1415, 1477, 1573–1577], although uncertainties in binary stellar evolution and pair-instability physics leave room for massive BH formation also through this channel [1394, 1578].

Spin magnitude and alignment are other quantities that ET can accurately measure, at least for the closest BBH mergers, to provide crucial insights about the unknown distribution of BH natal spins and the origin of the merging binary, despite the large uncertainties in stellar dynamics and evolution, and in the physics of stellar explosions [1421, 1579–1581]. Isolated BBHs are predicted to have mildly aligned spins, depending on the impact of SN explosions on the binary orbit [1579, 1582, 1583], and the establishment of precessional instabilities that can completely change the initial spin configuration (e.g., [1413, 1580]), whilst dynamical BBHs should have randomly oriented spins, unless some effect efficiently aligns them, e.g. like disk torques in AGN disks [1584].

Eccentricity probably is the most representative parameter of the dynamical channel. The isolated channel largely produces nearly circular mergers at $f > 1\,\mathrm{Hz}$. The eccentricity of dynamically assembled CBCs, gravitational-wave captures, and hierarchical triple systems, instead, can attain high values ($e > 0.9$) depending on the processes that affected the binary evolution. ET can measure eccentricities above $e > 0.01$ with accuracy at 1% level at redshift $z \lesssim 0.1$ [16, 1585], making it possible to identify mergers coming from high-energy dynamical

JCAP03(2026)081

interactions in dense star clusters, e.g. GW captures or collisions from resonant interactions in dense star clusters, or from dynamics in isolated triples.

4.2 Merger rate density of CBC across cosmic time

A common metric of the capabilities of GW detectors for population studies, which demonstrates the promise of next-generation detectors, is the fraction of the population that can be detected above a certain signal-to-noise (SNR) threshold as a function of redshift. The upgraded network of current detectors (Advanced LIGO, Advanced Virgo, and KAGRA with sensitivity curves as shown in [1586]) will be able to detect complete population of stellar BBH mergers with SNR ≥ 10 up to $z \sim 0.1$ and only up to $z \sim 0.01$ for the lower mass BNS mergers [107, 1586]. Therefore, even the upgraded network of current GW detectors will provide limited insight into the evolution of CBC properties through cosmic history. As we discuss in this section, this dependence encodes valuable information about the formation and evolution of stars and stellar multiples in environments very different from our cosmic neighborhood. It also probes the cosmic history of star clusters and galaxies. In addition, constraints on the evolution of the merger rate at redshifts $z > 2$ (above the peak of the cosmic star formation history [1587]) may prove key to overcoming current degeneracies in the astrophysical interpretation of the population properties of BBH mergers.

Although efforts are made to constrain the evolution of the CBC merger rate with current telescopes through sources such as gamma-ray bursts, many challenges (such as understanding selection effects, source classes, and environments) limit our ability to constrain the CBC merger rate even at small redshifts, let alone at $z \gtrsim 2$ [1571]. Such constraints can be obtained with next generation GW detectors. Iacovelli et al. [1167] estimate that ET alone can detect 100% of the BBH (BNS) mergers with SNR ≥ 12 up to $z = 1$ ($z = 0.2$). For the network of at least two next generation GW detectors, the complete BBH (BNS) population can be detected up to $z \approx 2$ ($z \approx 0.3$) [107, 1167]. Moreover, more than 90% of the BBH population can still be detected with SNR ≥ 12 out to $z = 20$. This redshift is more than a factor of two higher than that of the most distant known electromagnetic signal associated with the formation of a stellar compact object [1588–1590] and further back in the history of our Universe than any galaxy has ever been observed [1591]. ET will allow us to map the BBH merger rate beyond the current limits on the onset of the cosmic star formation and to access the unexplored epoch of the formation of the first stars and the first galaxies with BBH mergers.

4.2.1 The key ingredients of compact binary coalescence rates

With the exception of primordial BH mergers (see section 4.6), CBCs detectable by ground-based GW detectors originate from compact objects left over from the evolution of massive stars ($\gtrsim 8M_\odot$). Given the short evolutionary timescales of such stars (a few $10^6 - 10^7$ yr), the formation rate of stellar BHs and NSs follows the overall cosmic star formation history. However, only a small fraction of those compact objects evolve into observable CBC. Furthermore, depending on the efficiency of the processes that bring the two compact objects to merger (see section 4.1), these events can occur with a wide range of time delays, $t_{\rm delay}$, with respect to the formation of their progenitor stars. These delays can range from a few Myrs to the age of the Universe $T_{\rm Hubble} \sim 14$ Gyr. Consequently, the observable CBC population

JCAP03(2026)081

contains a mixture of systems formed throughout the Universe: at different times, with different chemical compositions, and in very different environments. Both the birth chemical composition and the environment in which stars evolve strongly influence the formation of CBCs and their population properties.

Birth chemical composition leaves imprint on stellar afterlives (CBC properties). Metallicity (i.e. the abundance of elements heavier than helium, Z) is a necessary initial condition for modeling the evolution of massive stars [1592] and stellar binaries/multiples, and influences the properties of stellar-origin compact objects such as masses and spins. Especially important is the abundance of iron, which determines the mass loss in stellar winds [1409, 1410, 1593–1595]. Iron-poor stars can end their lives as heavier black holes [1596], whose mergers lead to stronger GW signals. Weaker wind mass loss reduces the amount of angular momentum removed from the stars, possibly allowing the formation of compact objects with higher spin magnitudes. Stellar winds also remove mass and angular momentum from the system's orbit, typically leading to wider binaries at higher metallicities. This can change the type of interaction the binaries undergo later in their evolution, which has a non-trivial effect on the formation of double compact objects and CBC rates. Metallicity appears to be particularly important for the formation of mergers involving stellar BHs, whose formation efficiency in isolated channels may be greatly enhanced at low metallicity [1199, 1371, 1374, 1575–1577, 1597]. In addition, certain CBC formation scenarios (e.g., chemically homogeneous evolution; see section 4.1.1.2) may operate exclusively for metal-poor progenitors. Modeling the CBC population requires specifying the birth metallicity distribution of the progenitor stars forming at different times.

Environment plays a crucial role in the formation of CBCs. Other differences in the environments in which stars evolve allow for unique merger formation channels [1598]) (see section 4.1). In sparse stellar environments (galactic field), CBC formation involves exchanges of mass and angular momentum between stellar companions in isolated binary/multiple systems. In regions with a sufficiently high density of stars and compact objects, dynamical effects can further influence the formation of CBCs. In the densest environments (e.g., globular/nuclear clusters), compact object binaries can efficiently assemble dynamically and possibly undergo multiple mergers. Further differences in the CBC formation are expected in the presence of gas (e.g., in AGN disks), or in the case of extremely metal-poor/metal-free progenitors (see section 4.7). Therefore, modeling the CBC population requires specifying the cosmic formation history of the progenitors in the considered type(s) of environment.

CBC population — a mixed bag of everything. The overall observable CBC population is likely a superposition of subpopulations formed in multiple channels, whose relative contributions are expected to vary over cosmic time. The resulting cosmic merger rate density for a certain type of double compact objects (either BBH, BHNS or BNS binaries) is the sum over the contributions from different environments:

$$R_{\text{merger, DCO}}(t_{\text{merger}}) = \frac{d^2 N_{\text{merger, DCO}}}{dt_s dV_c}(t_{\text{merger}}) =$$
$$= \sum_{\text{env}} \int dZ \int_0^{t_{\text{merger}}} dt_{\text{delay}} \left(\frac{dM_{\text{SFR}}}{dt_{\text{form}} dV_c dZ}(t_{\text{form}}, Z) \right)_{\text{env}}^{(i)} \times \left(\frac{d^2 N_{\text{form,DCO}}}{dM_{\text{SFR}} dt_{\text{delay}}}(Z) \right)_{\text{env}}^{(ii)} \quad (4.1)$$

JCAP03(2026)081

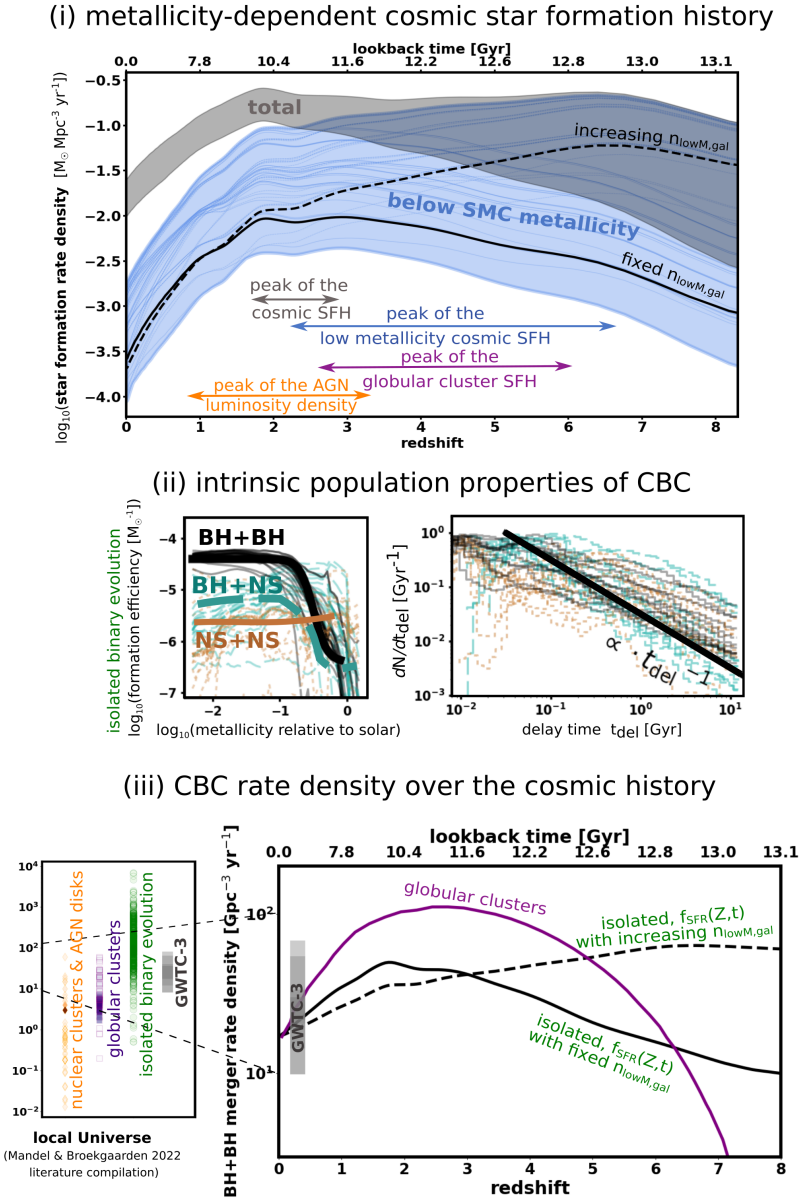

Figure 62. The key ingredients of compact binary coalescence rates. *Top:* star formation rate density (gray — total, blue — at metallicity lower than in the Small Magellanic Cloud) as a function of redshift/lookback time, spanned by observation-based $f_{\rm SFR}(Z,t)$ models from [1599, 1600]. Solid and dashed black lines show variation in the evolution of the low-metallicity Star Formation History (SFH) due to the uncertain high redshift evolution in the number density of low-mass galaxies ($\rm n_{lowM,gal}$). The arrowheads indicate the predicted range of redshifts for the peak of the star formation history in various types of environments and peak of the AGN luminosity density. *Middle:* $\eta_{\rm form}$ and delay-time distribution (DTD) illustrative of merging BBH (black), BHNS (turquoise) and BNS (brown) formed in isolated binary evolution channel. Thick lines: simplified main trends found in the literature. Thin lines: $\eta_{\rm form}$ and DTD for example binary population synthesis model variations from [1371] (left) and [1601] (right, normalised to the same value at peak) showing a diversity of shapes. *Bottom left:* literature compilation of the local BBH $R_{\rm merger}$ from [1571]. *Bottom right:* BBH $R_{\rm merger}$ redshift evolution examples normalised to the same local rate. Black dashed/solid lines — calculated using $f_{\rm SFR}(Z,t)$ variations corresponding to those shown as black dashed/solid lines in the top panel and the $\eta_{\rm form}$ and DTD shown as black lines in the middle panel. Purple line — example BBH $R_{\rm merger}$ for globular cluster channel from [1602].

JCAP03(2026)081

where t_s is the time in the source frame of the merger, V_c is the comoving volume, $t_{\rm merger} = t_{\rm form} + t_{\rm delay}$ and Z stands for metallicity. The term (ii) in the second parenthesis describes the *intrinsic* properties of the CBC populations. Specifically, $d^2N_{\rm form,DCO}/dM_{\rm SFR}dt_{\rm delay}$ is the number of binary compact objects that form per unit stellar mass and merge per unit delay time with $t_{\rm delay} < T_{\rm Hubble}$. In general, term (ii) depends on the formation channel/environment (e.g. field, globular cluster with certain properties). We can call merger efficiency the term $\eta_{\rm form,\ DCO} = dN_{\rm form,\ DCO}/dM_{\rm SFR}$ and delay time distribution (DTD) the term DTD $= dN_{\rm form,\ DCO}/dt_{\rm delay}$.

For a population of field stars formed with the same chemical composition, $\eta_{\rm form}$ and DTD depend on factors such as the fraction and initial parameters of stellar binaries/multiples, their evolution and interactions (mass transfer, tides), core collapse physics [1371, 1383, 1597, 1603, 1604]. For the CBC population formed in dense environments, the initial cluster properties (density profile, mass, binary fraction) can override the effects of stellar evolution on $\eta_{\rm form}$ and DTD [1547]. The term (i) in the first parenthesis of eq. (4.1) describes the cosmic volume-averaged star formation rate density at a given time and metallicity that ends in the considered type of environment (section 4.2.2). Its role is to weight the intrinsic population properties according to the chemical and star formation history representative of that environment. Term (i) is sensitive to factors such as the chemical evolution of galaxies, the physics of star formation and cluster formation history [1604].

The interpretation challenge. Many of the factors that go into the $R_{\rm merger,\ DCO}$ calculation are subject to large uncertainties. Taken together, this leads to a wide range of model CBC rate predictions in the literature (see [1571] and references therein). Strikingly, these predictions span a range that is orders of magnitude larger than the current GW-based constraints on the local $R_{\rm merger}$. This is the case for all CBC types, but is particularly striking for the BBH merger rate $R_{\rm merger,BBH}$, which is the best measured. The lower left panel of figure 62 shows that the GW constraints already rule out most current models, which tend to overestimate $R_{\rm merger,BBH}$ (especially when considering the possible contribution from multiple formation channels). However, the astrophysical interpretation of this fact, and hence the lesson to be learned from it, is unclear. The interpretation of these constraints is challenging because, even when considering a single CBC formation channel, $f_{\rm SFR}(Z,t)$ (term i), $\eta_{\rm form}$ and DTD (term ii) degenerate into $R_{\rm merger}$. In particular, different combinations of modeling assumptions about terms (i) and (ii) and the relative contributions of merger formation channels operating in different environments can lead to similar $R_{\rm merger}$ in the local Universe. The accuracy of local $R_{\rm merger}$ measurements for each type of CBC will continue to improve with ongoing and future GW observations, narrowing the overall parameter space of viable models. However, information on the redshift dimension is likely to be required to resolve the degeneracies in the interpretation. The role of ET constraints on the CBC rate in addressing this challenge is twofold:

- First, ET will provide joint constraints on the merger rate of all BBH, NSBH and BNS out to at least $z \sim 1$, mapping the rate evolution for all CBCs over the bulk of the cosmic history. This joint measurement is key: although BBH, BNS and BHNS are expected to be sensitive to different modeling uncertainties (e.g. due to the mass

JCAP03(2026)081

dependence of stellar evolution or the efficiency of dynamical merger formation), one must be able to reproduce $R_{\rm merger}(z)$ of all three from the same metallicity dependent cosmic star formation history.

- Second, ET will constrain the BBH merger rate well beyond the peak of the cosmic star formation history, where the uncertain factors associated with the environment (term (i)) are likely to dominate and lead to divergent $R_{\rm merger,BBH}(z)$ predictions, and they may affect the mass-specific rate even more strongly, see section 4.3 on mass distribution. These factors, discussed further in the following subsection 4.2.2, could potentially be constrained with the Einstein Telescope.

4.2.2 Part (i): cosmic star formation history as a function of metallicity and environment

Each subsequent generation of stars forms with broadly different metallicities. Their exact chemical composition depends on the complex interplay between the timing and metal yields of enrichment events, the mixing of metals in the interstellar medium, metal-poor inflows and metal-rich outflows. These processes shape the chemical evolution of individual galaxies. Their combined evolution determines the metallicity dependent cosmic star formation history $f_{\rm SFR}(Z,t)$, which characterises term (i) in eq. (4.1) for stars in the field and young/open clusters. The fraction of $f_{\rm SFR}(Z,t)$ forming in massive bound clusters (the progenitors of today's globular clusters), and the properties of these clusters, are expected to vary with the physical conditions in the local star-forming environment. Such factors further affect term (i) in eq. (4.1) characterising CBC progenitor formation in dense environments. The possibility of enhanced dynamical BBH merger formation in galactic nuclei (nuclear star clusters, gaseous AGN disks) introduces yet another class of environments with uncertain cosmic formation history. In principle, all environments characterised by different cosmic star formation histories can leave a unique imprint on the redshift evolution of the BBH rate, which can potentially be unravelled with future GW data.

4.2.2.1 Metallicity-dependent cosmic star formation history. Metallicity-dependent cosmic star formation history can be derived by combining statistical galaxy properties constrained by galaxy surveys [1249, 1599, 1600, 1605, 1606] or extracted from cosmological simulations of galaxy evolution [1607–1611]. Mixed approaches and simplified analytical prescriptions for the birth metallicity distribution of stars normalised to the chosen cosmic SFH are often used in the context of GW source population modeling (see [1604] for a recent discussion and comparison of literature assumptions).

The limitations of current methods result in $f_{\rm SFR}(Z,t)$ being particularly poorly constrained at low metallicity and high redshift (figure 62, top panel). Due to limited resolution, low-mass and starburst galaxies, which are crucial for low-metallicity star formation, are currently not accurately described in cosmological simulations. Many processes that are key to chemical evolution (e.g., enrichment by different types of supernovae, feedback processes) rely on prescriptions with poorly constrained parameters. Studies of the effects of such parameter choices in the full cosmological volume are limited by the high computational cost. Empirical bounds on $f_{\rm SFR}(Z,t)$ can be derived by combining observational distributions

JCAP03(2026)081

of galaxy properties (star formation rate, gas phase metallicity, stellar mass) and number statistics [1249, 1599, 1600, 1605, 1606]. These are increasingly incomplete at high redshift and low mass, i.e. for typically metal-poor galaxies. Constraints on the gas-phase metallicity are typically inferred from the oxygen abundances, which have large systematic uncertainties [1612, 1613] that translate directly into the uncertainty in $f_{\rm SFR}(Z,t)$ (see blue range in figure 62, which is based on oxygen abundance measurements). These systematics are one of the dominant factors driving the $f_{\rm SFR}(Z,t)$ uncertainty at low redshifts. Furthermore, the metallicity dependence of stellar evolution (and CBC formation) is thought to be primarily driven by iron. While constraints on gas-phase oxygen abundances are rapidly becoming available for much larger samples and redshifts, constraints on iron abundances in the star-forming material are scarce and likely to remain a challenge. Consequently, oxygen is often used as a proxy for iron abundance. However, the two elements are produced by sources operating on different timescales and the link between them is not straightforward — failure to account for that can lead to significant errors [1614].

The case for next generation GW detectors. Combined, the issues discussed above lead to a wide range of observationally allowed $f_{\rm SFR}(Z,t)$. This uncertainty cannot be ignored when interpreting the GW-based CBC population constraints, as the assumed $f_{\rm SFR}(Z,t)$ can strongly affect the model CBC properties, especially $R_{\rm merger}$ [1249, 1371, 1375, 1390, 1597, 1603, 1604, 1615, 1616]. This is particularly important for BBH mergers, where $f_{\rm SFR}(Z,t)$ alone can affect the local merger rate by more than an order of magnitude. If the strong low-metallicity preference of the BBH $\eta_{\rm form}$ seen in isolated channels is correct (black line, middle left panel in figure 62), the low-metallicity cosmic star formation history becomes the determining factor for the high redshift $R_{\rm merger,BBH}$ of such formed BBH mergers. This part of the $f_{\rm SFR}(Z,t)$ is shaped by the uncertain properties of low-mass and faint galaxies [1600], which map to a distinct $R_{\rm merger,BBH}$ evolution at redshifts >2 (compare the upper and lower panels of the figure 62). Constraints in this regime will provide a potential new way, complementary to electromagnetic observations, to study cosmic star formation, the early (iron) enrichment history and the properties of low-mass galaxies in the reionisation epoch [1604, 1617–1619].

Different types of mergers are expected to have a different $\eta_{\rm form}$ dependence on metallicity (figure 62, middle left panel), and hence their $R_{\rm merger}(z)$ may probe different parts of $f_{\rm SFR}(Z,t)$. Given the exciting prospect that the properties of BBH mergers will be mapped to $z > 10$ by the next generation GW detectors, these systems received the most attention in the literature as probes of cosmic history. However, the interpretation of the redshift evolution of BBH mergers is complicated by the potential competing contributions of different formation channels. This is less likely to be the case for mergers involving NS (see section 4.1), where isolated binary evolution is thought to dominate [1571, 1598]. While the GW constraints will not be available for the lower-mass BNS and BHNS at such high redshifts as for BBH mergers, their $R_{\rm merger}$ will be measured for most of cosmic history. Due to the expected weak metallicity dependence of BNS formation, their $R_{\rm merger}(z)$, modulo the effect of the DTD, is likely to track the total cosmic SFH (i.e. $f_{\rm SFR}(Z,t)$ integrated over all metallicities). BHNS formation is found to be enhanced at low metallicity, although less so than BBH. This makes the relative rate of BNS and BHNS mergers another promising probe of $f_{\rm SFR}(Z,t)$ [1371, 1604].

JCAP03(2026)081

4.2.2.2 Cluster formation history and properties. Both observational [1620–1622] and theoretical studies [1623–1625] indicate that the efficiency of cluster formation and their properties depend on the star forming conditions. The emerging consensus is that denser and more actively star-forming regions (such as those found in local starbursts [1626] and in the early Universe [1627, 1628]) favor the formation of massive and dense star clusters that can remain bound and evolve into today's globular clusters. Conversely, unclustered star formation leads to stellar systems that dissolve on short timescales and/or evolve into less dense open clusters. However, the full picture, from star formation through young clusters (where isolated CBC formation dominates) to the potential globular cluster stage (where dynamical interactions drive the CBC), remains fragmentary. This evolution is challenging to model because of the variety of spatial and temporal scales that need to be considered as clusters co-evolve with their host galaxies (but see [1629, 1630], for the recent efforts in the GW context). Related, the observational link between globular clusters and their progenitors is unclear because of their long history during which clusters can lose mass or dissolve completely.

Nevertheless, it is clear that only a fraction of $f_{\rm SFR}(Z,t)$ will eventually end up in environments where dynamical CBC formation becomes efficient. Given the properties of local globular clusters [1631, 1632] and the conditions that favor the formation of their progenitors, this fraction is expected to be higher at higher redshifts and lower metallicities. Furthermore, the efficiency with which CBCs can be dynamically produced depends on the uncertain distributions of initial cluster properties [1547, 1633–1636]. In other words, term (ii) in eq. (4.1) is sensitive to cluster characteristics, such as their masses and densities/half-mass radii. Calculating the total $R_{\rm merger}$ from cluster environments requires summing over the contributions from clusters with different characteristics.

Finally, we note that while dynamical formation in globular clusters can make a substantial contribution to the overall BBH merger rate, this is less likely to be the case for BNS and BHNS mergers. Their lower masses make them less likely to reside in cluster central regions where dynamical interactions are frequent [1459] and natal kicks associated with NS formation cause many of them to escape the cluster [1637] (see section 4.1.2). The potential imprint of the dynamical formation on other population properties of BBH mergers (mass, effective spin and eccentricity distributions) further motivates the focus on this class of CBC in the literature in the context of this channel (see section 4.1.3).

The case for next generation GW detectors. Both the possibility that the majority of today's globular cluster progenitors formed within the first Gyr of the Universe, and the possibility that the majority formed near the peak of cosmic star formation are considered in the literature. Such scenarios could potentially be discriminated with the $R_{\rm merger,BBH}$ constraints provided by the next generation GW detectors [1638, 1639].

Several authors discuss the promise of future GW data to jointly constrain the formation history of globular clusters and some of their initial properties [1547, 1639]. It is important to note that GW data alone cannot constrain all these uncertain properties, since many of them are degenerate in BBH $R_{\rm merger}$ (e.g. the distribution of virial radii and the cosmic formation rate of globular clusters). However, it can provide complementary information to improve constraints from other studies, at least as long as the subpopulation of cluster-formed

JCAP03(2026)081